8-23-2020

Numerical simulation and evaluation for the airflow field of surface ship

Wenxuan Ma

WORLD MARITIME UNIVERSITY

Dalian, China

NUMERICAL SIMULATION AND EVALUATION FOR THE AIRFLOW FIELD OF SURFACE SHIP

By

MA WENXUAN

The People's Republic of China

A dissertation submitted to the World Maritime University in partial Fulfillment of the requirements for the award of the degree of

MASTER OF SCIENCE
In
MARITIME SAFETY AND ENVIRONENT MANAGEMENT

2020

DECLARATION

I certify that all the material in this dissertation that is not my own work has been identified, and that no material is included for which a degree has previously been conferred on me.

The contents of this dissertation reflect my own personal views, and are not necessarily endorsed by the University.

Signature: Ma Wenxuan

Date: June 26th 2020

Supervised by: Professor Chang Xin

Supervisor's affiliation: Dalian Maritime University

ACKNOWLEDGEMENT

As one of the fruits of my study in MSEM during the year 2019-2020, this work's inspiration and knowledge base come from the lecture and assignment from all Professors. So, I would like to thank them who enlightened me and aroused my interest in Naval Engineering.

I would also like to express my sincere gratitude for the MSEM program and the project team, Pro.Chang Xin, for providing a reasonable and high-standard study system, strict management system and efficient logistics system, from which I constructed a knowledge system and a useful way of thinking. Those two constitute the basis for this paper.

I also appreciate my classmates, the fruitful discussions we had over many subjects, and the most memorable time we have shared together.

I also would like to say to my family and friends, especially my parents, thank you for your patience and support, without you, I cannot be engaged in study with few distractions.

ABSTRACT

Title of Dissertation: **Numerical Simulation and Evaluation for the Airflow Field of Surface ship**

Degree: **Master of Science**

The complex airflow of surface ships will directly interfere with the aerodynamic characteristics and maneuverability of ship-borne helicopters. It affects the takeoff and landing safety of ship-borne helicopters and needs to be considered in ship design.

The airflow of surface ship is a multi-factor coupled problem; if only an isolated ship is considered, the result will be deviated from the reality, but it is simple enough for quick forecasting. Coupling simulation is more computationally complex, but if there is a feasible solution that can realize the real-time dynamic coupling simulation, it will be possible to calculate the helicopter's manipulation and response accurately, and support the alternative evaluation.

Based on the above methods, this article has completed the following work:

Firstly, various turbulence models and numerical methods are compared and selected; a numerical simulation method based on CFD for later research is established.

Secondly, the numerical simulation of an isolated ship's airwake is carried out, and accuracy is verified by scaled model LHA. The vortex and velocity distribution of surface ship are analyzed under different wind conditions. The airwake characteristics of rapid prediction are achieved.

Finally, the numerical simulation of ship-helicopter coupling airwake is carried out. This paper selects the overlapping-virtual disk grid, using the ROBIN rotor-body aerodynamic interaction test, to verify the accuracy. The dynamic changes of airflow and aerodynamic components are successfully captured, thus proving that this method is feasible.

The conclusions obtained in this paper may be used as reference for simulation calculations and alternative evaluations of ship's airflow field.

KEYWORDS: numerical simulation; evaluation; surface ship; ship-borne helicopter; airflow; ship-helicopter coupling

TABLE OF CONTENTS

LIST OF TABLES

LIST OF FIGURES

LIST OF ABBREVIATIONS

2D/3D	2/3-Dimentional
AV	Attacker vertical
CFD	Computational Fluid Dynamics
CH	Carrier Helicopter
CPF	Canadian Patrol Frigate
CVN-73	USS George Washington
CVN-76	USS Ronald Reagan
DD-963	USS Spruance Destroyer
DDG-81	USS Winston S. Churchill
DES	Data Encryption Standard
DNS	Direct numerical simulation
DOF	Degree of freedom
ELECTRE	Elimination Et Choice Translating Reality
LES	Large eddy simulation
LHA	Landing Helicopter Assault
LPD-17	San Antonio-class amphibious transport dock
MAUT	Multi-attribute Utility Theory
NASA	National Aeronautics and Space Administration
NAWC	Naval Air Warfare Center
N-S	Navier-Stokes
PIV	Particle image velocity measurement
RANS	Reynolds-averaged Navier-Stokes equations
RKE	Realizable $k-\varepsilon$ model
RNG	Renormalization Group
SFS	Simple frigate shape
SKE	Standard $k-\varepsilon$ model
TOPSIS	Technique for Order Preference by Similarity to Ideal Solution
V-22	Boeing Bell V-22

CHAPTER 1 INTRODUCTION

1.1 Research background and significance

Surface ships refer to ships that are sailing, operating and fighting on the surface of the water, such as destroyers, patrol ships, etc. The tonnage of surface ships can range from dozens to 100 thousand tons of ships; they can be equipped with complex ship borne helicopters and missiles to provide fire support for land.

For a long time, surface ships have been valued and developed by many countries for their excellent tactical flexibility, various operational purposes or the strong ability to transport soldiers and equipment. In 2018, China has achieved the highest annual launching record of 27 warships, far more than those of other countries.

(a) Aircraft carrier Liaoning

(b) Arleigh Burke Class Destroyer

(c) Wasp-class amphibious assault ship

(d) Admiral Gorshkov Class Frigate

Figure 1-Figure of surface ships in different countries

Source: Internet

Considering the surrounding international situation of China, the development and

construction of surface ships is undoubtedly of a strategic significance to stabilize the situation, expand regional influence, and solve disputes such as the Taiwan issue and the Diaoyu Island issue.

When a ship is sailing, the air flows through the ship's hull, which will form a complex and changeable airflow. Because some surface ships carry ship-borne helicopters, the airflow and environmental characteristics on the deck, especially near the take-off and landing points, will directly affect the aerodynamic and control characteristics of the ship-borne helicopters. Therefore, how to provide a safe airflow environment for the ship-borne helicopters is one of the key issues to be considered in the design of surface ships.

Based on this background, it is of practical significance to study the structural characteristics of the airflow of surface ships, to realize the prediction of the airflow characteristics and the comprehensive evaluation of the ship airwake scheme.

1.2 Research methods and ideas

1.2.1 Research methods

There are two main methods for studying ship's airflow, one is using the computer to carry out numerical simulation and calculation based on the CFD technology, the other is to use a real ship or scale model to carry out wind tunnel test.

Before the CFD technology was used, most researches were using the second method. Actually, it is very difficult to carry out practical airflow measurement at sea because the different wind directions and speeds. Secondly, some special wind requirements are hard to meet. Thirdly, it costs too much and comes with great risks.

Relatively speaking, wind tunnel experiments can control the airflow condition more

accurately, and also make other factors easier to manage. However, the wind tunnel experiment is difficult to guarantee the accuracy. Also, it is hard to measure some airflow areas and physical quantities directly by test.

The numerical simulations based on the CFD technology can solve the above problems very well. Also, it can obtain any local conditions and quantities of the airflow. For now, this method is often used for a preliminary analysis, and then combined with the sea or wind tunnel test, the results will be verified and further analyzed. These two steps complement each other, and form a relatively complete research method system for ships' airflow.

1.2.2 Research ideas

Ship’s airflow is actually a multi-factor coupled field. There are two main ideas for ship’s airflow study. One is only to study airflow characteristics on an isolated ship. The second one is to study the coupling airflow. Apparently, the first one is deviated from the reality, so the results may lose its trueness, but it does lower the experiment cost, shorten the calculation time and under some circumstances would bring useful conclusions. The second one is more realistic, with higher authenticity and credibility, but it comes with high computational burden and experiment difficulty, easy to be restricted by resources and test conditions.

1.3 Research status at home and abroad

1.3.1 Numerical simulation and evaluation

1.3.1.1 Researches on isolated ships

In numerical simulation and evaluation, most researchers choose to set aside ship-helicopter coupling to simplify the calculation, only study on the isolated ship’s

airflow. The simulation of turbulence is very important in ship's airflow study. There are three main ways: DNS, RANS and LES.

For the application of RANS, Tai and Carico (2015) used RANS to simulate the DD-963 ship airflow; Syms (2004) also finished a steady calculation by RANS, and explained that the difference between the calculation and test is from the fluid instability; Bogtad et al. (2012) by considering ship's airflow as ideal fluid, obtained 6 different ships' airflows through steady simulation and apply their results on the simulator of ship-borne helicopters; Zan (2015) points that the accuracy of time from unsteady method is very important for the flight simulator airflow. Also, the time-varying wind direction must be considered into the simulation.

In China, Gao Ye et al. (2013) who carried out research on CVN deck vortices structure characteristics found that the shape and location of the super-structure would affect the intensity and location of the vortices behind the deck; Lu Chao et al. (2009) from China Ship Development and Design Centre who simulated the airflow of two different flight decks on one platform through RANS, demonstrated the 2D/3D streamlines of different laying-out; Zhao Yongzheng (2012) used RANS simulated the airflow from upper deck though both steady and unsteady situation, gave the results of superstructure in different positions, and emphatically analyzed the velocity distribution on the runway of ship-borne helicopters.

Regarding to the LES method, Camelli and Lohner (2013) simulated the airflow of LPD-17; Polsky (2013) studied the influence of boundary layer and grid mass on the calculation results of an air flow field under 90 degrees wind direction, and further compared the differences between the results from the reduced and real scale models; Arunajates et al. (2004) used LES to simulate the general LHA amphibious attack ship model, and compared the difference from the steady and unsteady simulation for

the ship airflow.

In China, He Shaohua and Liu Dongyue (2015) from the Naval Equipment Research Institute used LES to simulate the SFS model. The results show that the airflow fluctuates strongly, and the results from unsteady and steady calculation are quite different in some ways. Liu Changmeng (2014) from Harbin Engineering University used the coarse grid of RANS to compare LES and other turbulence models, and the results show that even though the LES with coarse mesh is not the best, it does have a nicer outcome.

In addition, the DES method, which combines RANS and LES, is also used in some researches. Forrest and Owen (2013) used DES to simulate and calculate the scale-up model of SFS-2, and verified the data with the wind tunnel test. The results are in good agreement, which shows the accuracy of DES method.

1.3.1.2 Researches on ship-helicopter coupling

Regarding the ship-helicopter coupling, Arunajatesan calculated the coupling characteristics of LHA amphibious assault ship with AV-8B aircraft under different height, and planning on doing more research on different vertical takeoff and landing aircraft coupling with ship. Tattersall et al. (1998) focused on the airflow over aft-located helicopter decks on conventional naval ships. Wakefield et al. (2002) simulated the airflow of a hovering helicopter rotor with ship structures and side winds. Polsky and Bruner (2000) simulated the coupling airflow of LHA with the downwash purling of Boeing bell V-22.

Starting from 2006, American Navy studied on the numerical simulation of ship-helicopter coupling, realized the dynamic coupling airflow simulation of ship borne helicopter hovering at a certain height on the deck and moving according to a

predetermined path.

In recent years, Alpman et al. (2007) added flight dynamics model to simulate the dynamic interference between ship and helicopter. Although it was using the simplified LHA model and the blade element theory, the results did show the necessity of coupling calculation. Lee and Silva(2013) used the moving-embedded grid method to study the pressure and velocity characteristics of the rotor-ship coupling airflow, which brings out the long calculating time disadvantage. Rajmohan et al.(2012) based on proper orthogonal decision, proposed a new method for the calculation of the rotor-ship coupled airflow. This method improves the calculation efficiency while ensuring its accuracy. The results show that the coupling airflow is significantly different from that of the isolated ship.

In China, research on the simulation of ship-helicopter coupling airflow is developing fast in recent years. In 2014, Sun Peng et al.(2015) and others of Dalian Maritime University studied the complex rotor-ship airflow with FLUENT, and the characteristics of coupling airflow in different wind directions; in 2017, Su Dacheng et al.(2017) and others developed a set of ship-helicopter coupling airflow simulation method based on RANS, and the results show that the influence of fuselage and tail rotor on ship's airflow is relatively small, so it can only consider the rotor to analyze the helicopter landing motion therefore improve the efficiency.

1.3.2 Wind tunnel and sea trial

1.3.2.1 Researches on isolated ship

In Russia, the development of large-scale ships would take nearly one month for ship model airflow characteristic test in wind tunnel, and a large number of tests and measurements will be carried out during the period of ships construction.

In the US, up to 2008, the Naval Aviation Department has completed the following research work on the test and measurement of isolated ships:

Full-scale sea tests were conducted on the amphibious assault ship LHA, aircraft carrier cvn-76, etc. ; scale model wind tunnel tests were conducted on the amphibious assault ship LHA, aircraft carrier CVN73, CVN-76, destroyers DDG-81, DD-963, frigate LPD-17, and some main mast and antenna structures.

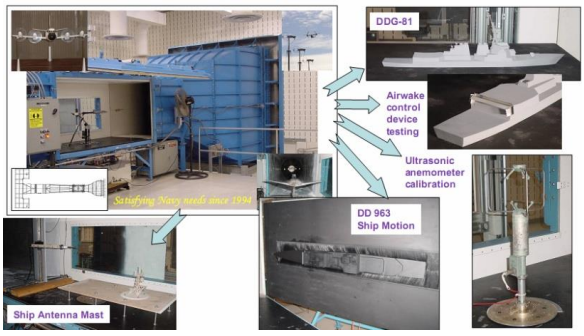

Figure 2-Low-speed wind tunnel equipment in NAWC

Source: Internet

1.3.2.2 Researches on ship-helicopter coupling

In doing the wind tunnel test, some researches try to consider the coupling effect of ship borne helicopter. In 2002, Zan studied the influence of CPF ship’s wind speed and direction on the helicopter engine. The results showed that in some cases, the ship airflow reduced the air intake of the engine, and reduce engine thrust significantly, which would burden the pilot's control. After that, Lee and Zan (2002) have continued to carry out wind tunnel tests to study the unsteady aerodynamic loads on the "Haiwang" helicopter’s fuselage under CPF ship’s airwake.

In the wind tunnel test of ship-helicopter coupling airflow, one famous project called V-22/ Ship/ Helicopter Aerodynamic Interaction Phenomena, carried out by NASA (Johnson, 2003), is shown in Figure 3.

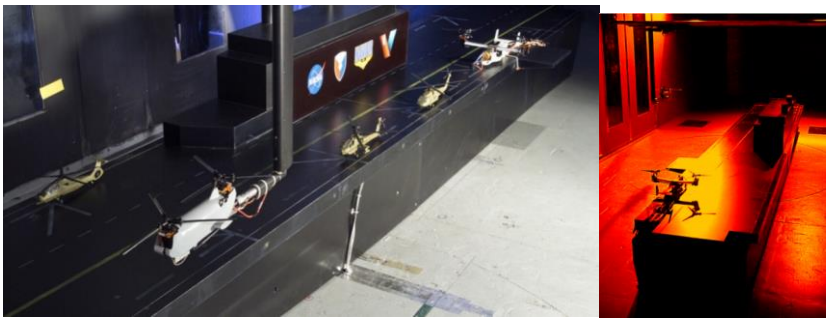

Figure 3-The model of ship-helicopter coupling in VASHAIP of NASA

Source-Author

The project originated from a ship borne aircraft compatibility test on LHA amphibious attack ship in 1999, V-22 tilt rotor aircraft overturned unexpectedly somewhere above the deck (Silva, 2004). Thus, the U.S. military conducted the Army/NASA/NAVAIR 1/48th-scale scale wind tunnel test in the Ames Research Center of NASA. The results are very helpful for studying the aerodynamic interference mechanism of LHA aircraft. This test determined the safety limit of V-22 landing wind condition, and studied the aerodynamic interference of multiple ship borne helicopter including V-22 and CH-46 on LHA (Wadcock, 2004; Yamauchi, 2003).

1.3.3 Alternative evaluation

The evaluation and optimization methods are constantly proposed beyond seas, including the Lagrange multiplier method, the steepest descent method, the linear programming, the nonlinear programming and the dynamic programming. In China, Lv Jianwei et al.(2005) introduced the theory of utility function into the evaluation of warship combat capability, and gave the value function expression of warship performance index. Li Ping, Huang Sheng, et al.(2005) studied the basic risk components in ship design and the relationship between them, gave the corresponding quantitative analysis method for each basic risk component, and

discussed the determination of risk criteria in risk analysis and decision-making process. In 2006, Lu Jianwei et al. (2006) established a comprehensive evaluation model of ship development scheme by applying the rough set theory, and verified the superiority of this algorithm. In recent years, Xiong Yunfeng(2007), Liu Chuanyun(2009), Hou Yuanhang(2012), Liao quanmi(2015), Zhang Xiuyuan(2016) and others are using such methods as the grey system theory, MAUT, TOPSIS, the combination of grey correlation degree and TOPSIS, improved ELECTRE and other methods to study the evaluation theory of the overall plan of the ship.

1.4 Limitations in China

According to the published literature in China, compared with foreign researches, the limitations in the numerical simulation and evaluation of large-scale ship's airflow are mainly as follows:

(1) At present, most of the domestic researches are only for isolated ships, which deviate from the reality, and the authenticity of the calculation results is not guaranteed;

(2) According to the progress and trend in foreign countries, it should be based on the realization of "real-time dynamics" and "ship-helicopter coupling", to obtain the aerodynamic response and balance control quantity of the helicopter for the ship's airflow, and to develop safe operating envelope, and take the quality of the safe operating envelope as the most important indicator for the ship's airflow scheme evaluation. At present, the domestic research has not reached this far.

1.5 Structure of this dissertation

Based on the current researches in China, the main contents of this paper are as

follows:

(1) Research background, research methods and status are analyzed and summarized

(2) Establish the numerical simulation method

According to the follow-up research, basic control equation of numerical simulation is given considering the calculation efficiency and accuracy. The turbulence simulation method, the space divergent method and the time discrete method are compared and selected.

(3) Carry out numerical simulation of an isolated ship

Without considering the ship-helicopter coupling, verify the accuracy of the numerical simulation method by using the small-scale LHA model. Then, according to the real scale surface ship, calculate and analyze the airflow under different wind speed and direction, and analyze different vortices and vertical velocity distribution of different landing path on the certain landing point under specific wind condition.

(4) Carry out the numerical simulation of the ship-helicopter coupling airflow

Compare and analyze different models, select the Overlapping-Virtual disk model. Using the ROBIN interference model to verify and obtain a numerical simulation example of the coupling airflow. Then compare the results of isolated airflow and coupling airflow, coupling calculation and isolated superposition, to illustrate the necessity of ship-helicopter coupling calculation. At the same time, by the numerical calculation of the coupling airflow, the change of the aerodynamic components of the helicopter during landing is obtained, which lays the foundation for the calculation of the safe operating envelope and the comprehensive evaluation of the airflow scheme of the ship.

CHAPTER 2 ESTABLISHMENT OF THE NUMERICAL SIMULATION METHOD

2.1 Introduction

This chapter will give the basic control equation of numerical simulation considering the calculation efficiency and accuracy. Compare and select a proper turbulence simulation method, space divergent method and time discrete method based on their advantages and application status, thus, a numerical simulation method is established for the follow-up study of ship airflow.

2.2 Numerical methods and physical models

2.2.1 Control equations

Any fluid flows must comply with physical conservation laws; there are three basic laws of conservation: mass, momentum and energy conservation. Correspondingly, there are three control equations in dynamic fluid:

2.2.1.1 Continuity equation

Based on the mass conservation law, the mass of the same fluid does not change during motion. From this, continuity equation can be deduced, it's differential from as follows:

$$\frac{\partial \rho}{\partial t} + \nabla \cdot (\rho V) = 0 \tag{2-1}$$

where ρ is the density of fluid; t means time, and V is the velocity of fluid.

During steady motion, $\frac{\partial \rho}{\partial t} = 0$, become:

$$\nabla \cdot (\rho V) = 0 \tag{2-2}$$

or

$$\frac{\partial(\rho V_x)}{\partial x} + \frac{\partial(\rho V_y)}{\partial y} + \frac{\partial(\rho V_z)}{\partial z} = 0 \tag{2-3}$$

Because ship's airflow in this paper has been considered as incompressible fluid, $\rho = const$, which means $\frac{\partial \rho}{\partial t} = 0$, so the continuity equation of incompressible fluid is shown as:

$$\nabla \cdot V = 0 \tag{2-4}$$

or

$$\frac{\partial(V_x)}{\partial x} + \frac{\partial(V_y)}{\partial y} + \frac{\partial(V_z)}{\partial z} = 0 \tag{2-5}$$

where V_x is fluid's x velocity component, V_y is fluid's y velocity component, V_z is fluid's z velocity component.

2.2.1.2 Equation of motion

Based on Newton's second law, the motion differential equation of viscous, compressible, Newtonian fluid--N-S equation is shown as:

$$\frac{dV}{dt} = F - \frac{1}{\rho}\nabla P + \upsilon \nabla^2 V + \frac{\upsilon}{3}\nabla(\nabla \cdot V) \tag{2-6}$$

where, F is the mass force per unit mass fluid, P is the resultant pressure of fluid, υ is kinematic viscosity.

For the airflow is incompressible, $\nabla \cdot V = 0$, so:

$$\frac{dV}{dt} = F - \frac{1}{\rho}\nabla P + \upsilon\nabla^2 V \tag{2-7}$$

or:

$$\left.\begin{aligned} \frac{dV_x}{dt} &= F_x - \frac{1}{\rho}\frac{\partial P}{\partial x} + \upsilon\nabla^2 V_x \\ \frac{dV_y}{dt} &= F_y - \frac{1}{\rho}\frac{\partial P}{\partial y} + \upsilon\nabla^2 V_y \\ \frac{dV_z}{dt} &= F_z - \frac{1}{\rho}\frac{\partial P}{\partial z} + \upsilon\nabla^2 V_z \end{aligned}\right\} \tag{2-8}$$

where F_x represents x component of unit mass force; F_y represents y component of unit mass force; F_z represents z component of unit mass force.

2.2.1.3 Energy equation

Based on the energy conservation law, the energy equation of a fluid is shown as:

$$\rho\frac{d(\frac{V^2}{2})}{dt} + \rho\frac{dU}{dt} = \rho F \cdot V + \nabla\cdot(PV) + \nabla\cdot(k\nabla T) + \rho q \tag{2-9}$$

where U represents internal energy per unit mass, F represents external force on unit mass fluid, k represents thermal conductivity, T is temperature, q is heat distribution function of unit mass introduced in unit time due to radiation or other reasons.

2.2.2 Turbulence model

2.2.2.1 Comparison and selection of basic turbulence simulation methods

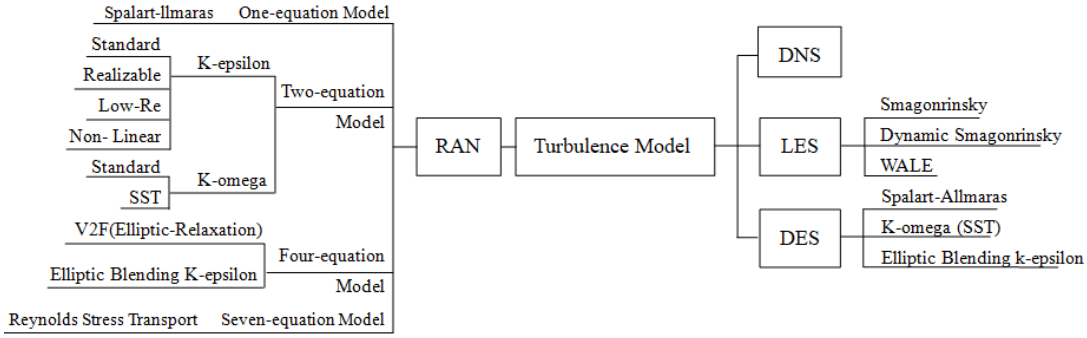

Figure 4-Classification of main turbulence simulation methods

Source: Author

It can be seen from Figure 4, for now the turbulence numerical simulation method can be divided into DNS, RANS and LES. After these, there are DES which is a combination of RANS and LES. Pros and cons on these three methods are shown in Table 1.

Table 1-Pros and cons of three turbulence simulation methods

Method	Pros	Cons
DNS	1. Direct numerical solution of NS equation, barring any artificial hypothesis or empirical parameter 2. No closed problems 3. Any physical quantity's transient time and space evolution can be obtained. 4. Turbulent flow structure can be shown clearly.	1. Higher requirement on computing resource and longer time on calculating 2. Restrain by computing resource, for now can only solve simply turbulence problems with small Reynolds number.
RANS	1. Lower requirement on computing, faster and results are more suitable for engineering 2. Easier to solve turbulence statistic when reasonable Reynolds stress model are gave. 3. Can solve engineering problems with large Re.	1. Different model for different turbulence. 2. Less consideration on kinematics and dynamics on vortices to reveal the flow mechanism. 3. There are problems on the numerical simulation of unsteady, large separation and reverse pressure gradient. 4. Poor universality and strong dependence on experience.

LES	1. Capable of describing small scale turbulent flow. 2. Calculation amount: RANS<LES<<DNS 3. Using non-uniform grids can minimize the number if grids, save computing resources and ensure sufficient calculation accuracy at the same time. 3. The grid scale is larger than turbulence scale to simulate details in turbulence development.	1. Dense grids come with large calculation. 2. High speed numerical processing capability are needed for a lot if data processing and solutions of nonlinear partial differential equations. 3. Only suit for simple shear and pipe flow.

Source: Author

From the above comparison, on solving ship-helicopter coupling problems, the RANS method is more suitable.

2.2.2.2 Comparison and selection of turbulence models under RANS

The advantages and disadvantages of the main turbulence models in terms of calculation time and accuracy are summarized in Table 2.

Table 2-Comparison of different turbulence models under RANS

Turbulence model	Advantages	Disadvantages
Reynolds stress model	Most accurate model, high universality and reliability	Very complex, a lot of differential equations to be solved and more time consuming
Algebraic stress model	Widely used, easier than Reynolds stress model and same calculation accuracy	Must satisfy the conditions required for diffusion and convection terms
Two-equation model	Widely used in engineering, simple, practical and less time consuming	Slightly lower accuracy and lower forecast ability on highly complex flow
Others	Simply model	Lack of universality and computing models are too simply for reliability.

Source: Author

For the large real-scale ship airflow studied in this paper, due to the large number of grids and the large amount of calculation, the comparison and analysis of the calculation time and accuracy of several turbulence models under RANS in the table above show that the two-equation turbulence models are more suitable for actual needs.

2.2.2.3 Comparison and selection of $k-\varepsilon$ models under two-equation

The advantages and disadvantages of several common two-equation turbulence models in RANS viscous vortex mode are summarized in Table 3.

Table 3-Comparison of three $k-\varepsilon$ models

Turbulence Model	Pros	Cons
Standard $k-\varepsilon$ Model	Widely used, appropriate amount of calculation	Poor prediction of strong separation flow, strong swirl flow and high pressure gradient flow
RNG $k-\varepsilon$ Model	Moderately complex flows such as jet, separation flow, secondary flow, swirl, etc. can be simulated	Poor simulation on strong swirl
Realizable $k-\varepsilon$ Model	Basically in accordance with RNG $k-\varepsilon$ model and can also simulate the circular jet problem.	Poor simulation on strong swirl

Source: Author

Compared with the other methods, RKE was proposed later. The transport equation for turbulent kinetic energy and dissipation rate of RKE is:

$$\frac{\partial(\rho k)}{\partial t}+\frac{\partial(\rho k u_i)}{\partial x_i}=\frac{\partial}{\partial x_i}\left[\left(\mu+\frac{\mu_t}{\sigma_k}\right)\frac{\partial k}{\partial x_i}\right]+G_k+G_b-\rho\varepsilon-Y_M \qquad (2\text{-}10)$$

$$\frac{\partial(\rho\varepsilon)}{\partial t} + \frac{\partial(\rho\varepsilon u_i)}{\partial x_i} = \frac{\partial}{\partial x_i}\left[\left(\mu + \frac{\mu_t}{\sigma_\varepsilon}\right)\frac{\partial\varepsilon}{\partial x_i}\right] + C_{1\varepsilon}\frac{\varepsilon}{k}C_{3\varepsilon}G_b + C_1\rho S_\varepsilon - C_2\rho\frac{\varepsilon^2}{k+\sqrt{\nu\varepsilon}} \tag{2-11}$$

Default values for some of these constants are shown in Table 4.

Table 4-Constants for Realizable $k-\varepsilon$ Model

C_μ	C_1	C_2	σ_k	σ_ε	$C_{1\varepsilon}$
$C_\mu = \frac{1}{A_0 + A_s U^* k / \varepsilon}$	$C_1 = \max\left[0.43, \frac{\eta}{\eta+5}\right], \eta = \frac{Sk}{\varepsilon}$	1.9	1.0	1.2	1.44

Source: Author

For the large-scale ship-helicopter airflow simulation in this paper, based on the comparison and analysis of the advantages and disadvantages of the three common turbulence models in the table above, the Realizable model is finally selected for the simulation.

2.2.3 Spatial discretization

In order to solve the control equation, the computational area space should be discretized, the continuous computational area in space is divided into many sub-areas to generate a grid, and then discretize the control equation on the grid.

At present, spatial discrete methods include the finite difference method, the finite element method, the finite volume method, the boundary element method, and etc. The CFD software STAR-CCM+ used in this paper is also spatially discrete based on the finite volume method.

Current discrete schemes mainly include first-order and high-order discrete schemes. Due to the CFD software STAR-CCM+, only the first-order upwind scheme and the second-order upwind scheme can be selected under the Reynolds average numerical

simulation method, while the second-order upwind diffusion term uses the central discrete scheme. Therefore, the following sections will briefly introduce the central difference scheme, the first-order upwind scheme and the second-order upwind scheme.

(1) Central difference scheme

The central difference scheme is to take the arithmetic mean values of upstream and downstream nodes as the physical quantities of interface, i.e. linear interpolation Equation. Central difference scheme cannot be used for general flow problems.

For a given uniform grid in one dimension, the physical quantity ϕ at the control volume interface is:

$$\phi_e = \frac{\phi_P + \phi_E}{2} \tag{2-12}$$

$$\phi_w = \frac{\phi_P + \phi_W}{2} \tag{2-13}$$

The integral transport equation for calculating the control volume at the P is:

$$F_e\phi_e - F_w\phi_w = D_e(\phi_E - \phi_P) - D_w(\phi_P - \phi_W) \tag{2-14}$$

By substituting Equation (2-16) and Equation (2-17) into Equation (2-18):

$$\frac{F_e}{2}(\phi_P + \phi_E) - \frac{F_w}{2}(\phi_P + \phi_W) = D_e(\phi_E - \phi_P) - D_w(\phi_P - \phi_W) \tag{2-15}$$

Introduced the discrete form of the continuous equation:

$$(D_w + \frac{F_w}{2} + D_e - \frac{F_e}{2} + F_e - F_w)\phi_P = (D_w + \frac{F_w}{2})\phi_W + (D_w - \frac{F_e}{2})\phi_E \tag{2-16}$$

By using k_W、k_E、k_P as the coefficients of ϕ_W、ϕ_E、ϕ_P, the discrete form of the convection-diffusion equation in the central difference scheme is shown as:

$$k_P\phi_P = k_W\phi_W + k_E\phi_E \tag{2-17}$$

where:

$$\left.\begin{aligned} k_W &= D_w + \frac{F_w}{2} \\ k_E &= D_e - \frac{F_e}{2} \\ k_P &= k_W + k_E + F_e - F_w \end{aligned}\right\} \tag{2-18}$$

(2) The first-order upwind scheme

The first-order upwind mode, i.e. the unknown physical quantities on the interface, is always taken as the value of the upstream node.

In the first-order upwind scheme, when the flow is in a positive direction, i.e.

$u_w > 0, u_e > 0$, there are:

$$\phi_e = \phi_P \tag{2-19}$$

$$\phi_w = \phi_W \tag{2-20}$$

By substituting Equation (2-23) and Equation (2-24) into Equation (2-18) and introducing the discrete form of continuous equation, the following results are obtained:

$$(D_w + D_e + F_w + F_e - F_w)\phi_P = (D_w + F_w)\phi_W + D_e\phi_E \tag{2-21}$$

When the flow is in the negative direction, then equation (2-25) becomes:

$$(D_w + D_e - F_w + F_e - F_w)\phi_P = D_w\phi_W + (D_e - F_e)\phi_E \tag{2-22}$$

In conclusion, the first order upwind convection-diffusion equation in the discrete form is shown as:

$$k_P\phi_P = k_W\phi_W + k_E\phi_E \tag{2-23}$$

where:

$$\left.\begin{aligned} k_W &= D_w + \max(F_w, 0) \\ k_E &= D_e + \max(0, -F_e) \\ k_P &= k_W + k_E + F_e - F_w \end{aligned}\right\} \tag{2-24}$$

(3) Second-order upwind scheme

The second-order upwind scheme can be seen as the first-order upwind, taking into account the curvature effect of distribution curve between nodes. In the second-order upwind scheme, only the convection term uses the second-order upwind scheme, while the diffusion term still uses the central difference scheme.

The principle of the second-order upwind node "windward" is shown in Figure 5.The grid in the graph is uniform and the shaded part is the control volume at the calculated node P.

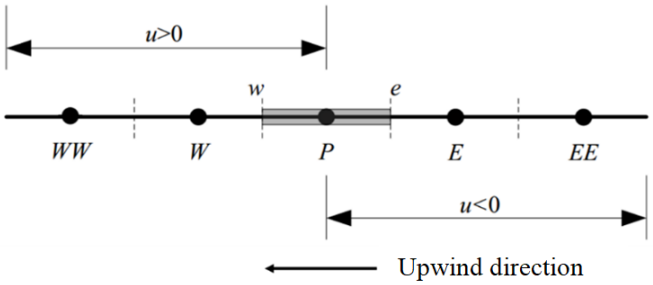

Figure 5-"Upwind" Principle of Second Order Upwind Scheme

Source: Author

When the flow is in a positive direction, i.e. $u_w > 0, u_e > 0$:

$$\phi_w = 1.5\phi_W - 0.5\phi_{WW} \tag{2-25}$$

$$\phi_e = 1.5\phi_P - 0.5\phi_W \tag{2-26}$$

By substituting Equation (2-29) and Equation (2-30) into Equation (2-18):

$$(D_w + D_e + \frac{3}{2}F_e)\phi_P = (D_w + \frac{1}{2}F_e + \frac{3}{2}F_w)\phi_W + D_e\phi_E - \frac{3}{2}F_w\phi_{WW} \quad (2\text{-}27)$$

When the flow is in the negative direction, then equation (2-31) becomes:

$$(D_w + D_e - \frac{3}{2}F_w)\phi_P = (D_e - \frac{3}{2}F_e - \frac{1}{2}F_w)\phi_E + D_w\phi_W - \frac{3}{2}F_e\phi_{EE} \quad (2\text{-}28)$$

In conclusion, the discrete form of the convection-diffusion equation of the second order upwind type is:

$$k_P\phi_P = k_W\phi_W + k_{WW}\phi_{WW} + k_E\phi_E + k_{EE}\phi_{EE} \quad (2\text{-}29)$$

where:

$$\left.\begin{aligned} k_W &= D_w + \frac{3}{2}\alpha F_w + \frac{1}{2}\alpha F_e \\ k_E &= D_e - \frac{3}{2}(1-\alpha)F_e - \frac{1}{2}(1-\alpha)F_w \\ k_{WW} &= -\frac{1}{2}\alpha F_w \\ k_{EE} &= \frac{1}{2}(1-\alpha)F_e \\ k_P &= k_W + k_E + k_{WW} + k_{EE} + F_e - F_w \end{aligned}\right\} \quad (2\text{-}30)$$

where:

$$\left.\begin{aligned} \alpha &= 1, \text{positive direction} \\ \alpha &= 0, \text{negtive direction} \end{aligned}\right\} \quad (2\text{-}31)$$

2.2.4 Time Discrete

For the transient calculation of the unsteady airflow in this paper, the control equation is discretized in time. Time discrete methods are generally divided into explicit time-marching method and implicit time-marching method.

A comparison of the advantages and disadvantages of the time-marching method is shown in Table 5.

Table 5-Comparative analysis of explicit and implicit methods

Time Discrete Method	Advantages	Disadvantages
Explicit time-marching	(1) Only one unknown number in each difference equation, which can be explicitly solved by direct calculation, so its relatively simple to calculate	(1) Once the grid size Δx is determined, then the time step Δt 's value must be limited by the stability condition and less than or equal to a certain value in order to maintain the stability. (2) When the grid is densely distributed, a small time step Δt will lead to long calculation time.
Implicit time-marching	(1) It can take larger and less time steps. (2) For some applications, although the implicit method takes longer to complete a time step, due to the small number of steps, the total running time may be less than that of the explicit method.	(1) Involves the calculation of large matrices and requires more complex calculations than the explicit method. (2) When the time step Δt is large, the truncation error will be large, and the implicit method may not be as accurate as the explicit method when tracking the strict transient changes.

Source: Author

The flow field near the surface ship in this paper will change dramatically; a more dense space grid is needed, so here choosing implicit method to greatly reduce the calculation time.

Therefore, based on the comparative analysis in table 2.6, this paper adopts the implicit time-marching method.

2.2.5 Initial conditions

The initial condition refers to the flow state of each point in the solved airflow at a

certain time (for example $t = t_0$). Since only the first derivative of time appears in the hydrodynamics equations, only the initial distribution of the physical quantities at the initial time is needed. For example:

For a given $t = t_0$,

$$\left.\begin{aligned} V(x, y, z, t_0) &= V(x, y, z) \\ P(x, y, z, t_0) &= P_0(x, y, z) \end{aligned}\right\} \tag{2-32}$$

For a steady flow, no initial condition is required.

2.2.6 Boundary conditions

Following part will general discuss the boundary conditions of the fluid-solid interface in ship airflow, i.e. the wall boundary conditions. If the fluid cannot pass through the solid wall and the flow does not separate, then for viscous fluid, there are

$$V = V_b \tag{2-33}$$

For ideal fluids, there are

$$V \cdot n = V_b \cdot n \tag{2-34}$$

where:

V is the velocity vector of fluid on the solid wall;

V_b is the velocity vector of the solid wall;

n is the unit vector in the external normal direction.

Equation (2-37) shows that no matter how fast the fluid moves, it always sticks to the solid wall contact surface due to viscosity, and the tangential velocity and normal velocity are the same, indicating that they are neither separated nor relatively sliding. Therefore, Equation (2-37) is also called no slip condition [53]. For the ship and

helicopter fuselage studied in this paper, the condition of no sliding wall is adopted.

Equation (2-38) shows that when ignore viscosity, there can be relative slip between two media as long as the normal velocity is continuous on the solid wall,

For this paper, the airflow is single-phase flow. The normal velocity at the interface remains continuous. Therefore, the water-air interface is treated as a sliding solid wall.

2.3 Motion Simulation Grid Technology

This section will briefly introduce and explain two motion simulation grids commonly used in commercial CFD software, Moving Overset Grids and sliding mesh.

2.3.1 Overlapping grid

The overlapping grid technology, also known as Moving Overset Grids technology, allows overlapping, nesting and overlaying between grids without tedious topological partitioning, thus reducing the difficulty of grid generation. When it comes to flow problems involving relative motion of multi-body, Moving Overset Grids can be used to establish a connection between the grids, which can be used to transmit the information of interface airflow in each region.

2.3.2 Sliding grid

Sliding grids allow relative sliding between adjacent grids, so grid surfaces do not need to be arranged on the interface. Compared with overlapping grid, slip grid method is fast and efficient. At present, the sliding grid method is mainly used for the numerical simulation of flow fields such as hovering rotors, fixed-wing propellers, wind turbines and engine blades.

The main calculation progress of the sliding grid method is shown in Figure 6.

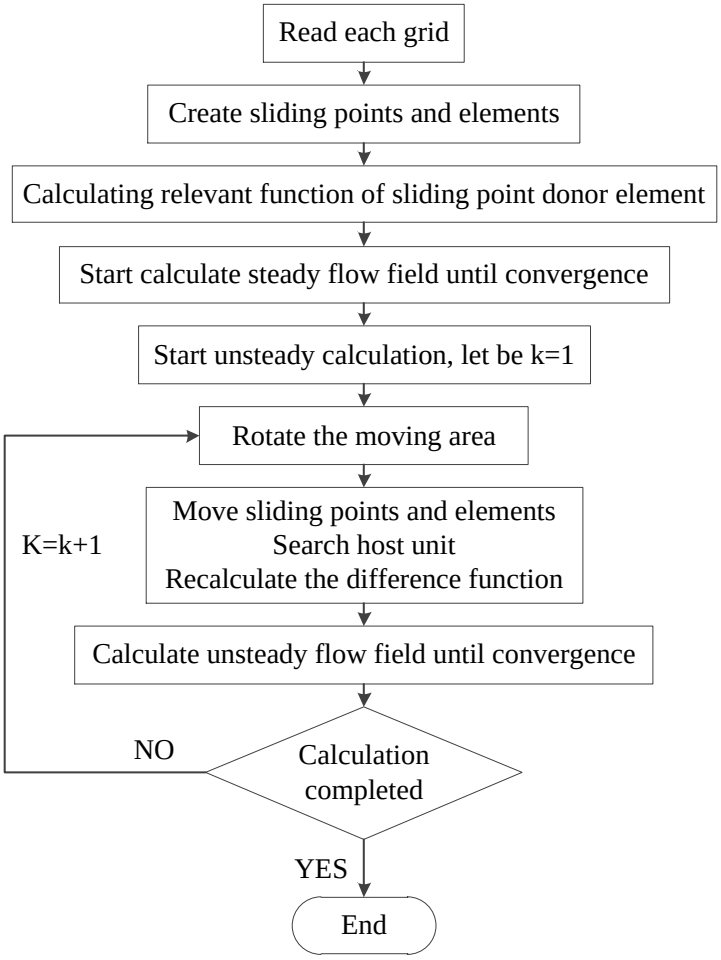

Figure 6-Calculation progress of sliding grid

Source: Author

2.4 Summary

In this chapter, according to the need of numerical simulation of ship airflow field in the follow-up study, the basic control equation was given, and the applicable range was compared and selected, advantages and disadvantages of turbulence simulation method, space-discrete method, time-discrete method, etc. were discussed. The numerical simulation method is established. The main contents and conclusions of

this chapter include:

(1) Three basic control equations, the mass conservation, the momentum conservation and the energy conservation are given.

(2) Realizable two-equation model under Reynolds Mean Simulation were used for turbulence simulation. The first-order upwind method is used for spatial discretization and the implicit unsteady method for time discretization. For ships and helicopters, use the non-slip wall boundary condition. Because this research belongs to single-phase flow, slip boundary condition should be used for seawater surface.

(3) Overlapping grid and slip grid techniques were introduce and explain, lay a foundation for dynamic coupling calculation of helicopter landing process.

CHAPTER 3 NUMERICAL SIMULATION OF ISOLATED SHIP AIRFLOW

3.1 Introduction

This chapter will analyze isolated ship airflow characteristics under different wing speed and conditions while verify calculation accuracy, without considering ship-helicopter coupling, the key point is to analysis the development and velocity distribution law of vortex under different wind conditions, and compare the vertical velocity distribution of different landing paths at a certain landing point under specific wind conditions.

3.2 Computational model and methods

3.2.1 Real scale computational model

The real scale ship computational model in this paper is a simplified copy of American Wasp-class amphibious assault ship, as shown in Figure 7, the principal dimension parameters is shown in Table 6.

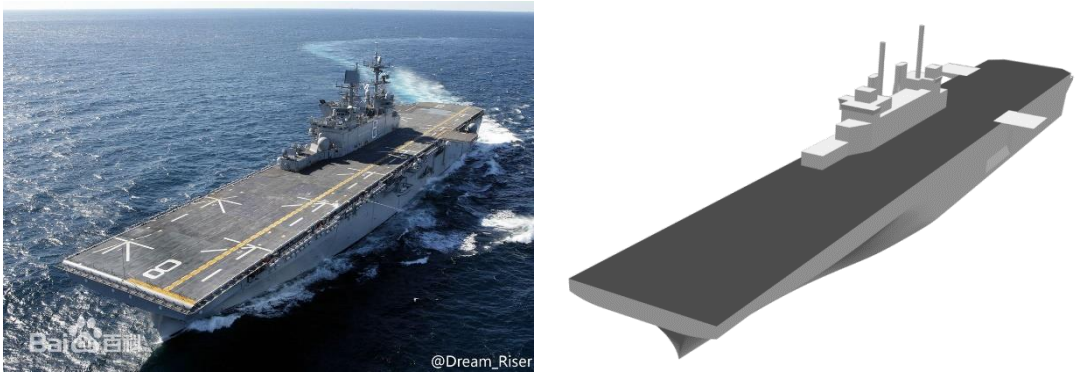

(a) Wasp-class amphibious assault ship (b) Real scale ship computational model

Figure 7-Real scale ship computational model

Source: Author

Table 6-Principal dimension parameters of real scale model

Flying deck length	256.4 m
Flight deck width	35.8 m
Height of water line from flight deck	19.8 m

Source: Author

Following the deck arrangement of the "Wasp-class" ship, there are six take-off and landing points from the bow to the stern, numbered A, B, C, D, E and F in turn, as shown in Figure 8.

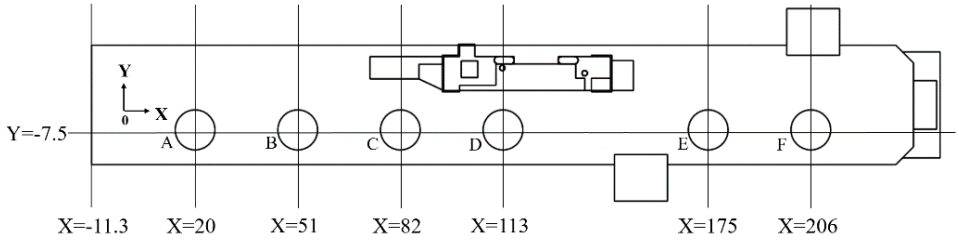

Figure 8-Distribution of Take-off and Landing Points in Real Scale Models (m)

Source: Author

3.2.2 Computing Domain and Grid Dividing

Sun Xiaodun (2007) proposed the concept of blocking rate when studying the selection of calculation domain for blunt body bypass flow.

$$\text{Blocking Rate}=\frac{\text{Maximum Frontal Area}}{\text{Cross Sectional Drainage Area}}$$

The computational domain size needs to keep blocking rate less than 3% according to the literature. Considering both the calculation accuracy and the number of grids, the main scale of the calculation domain is shown in Figure 9.

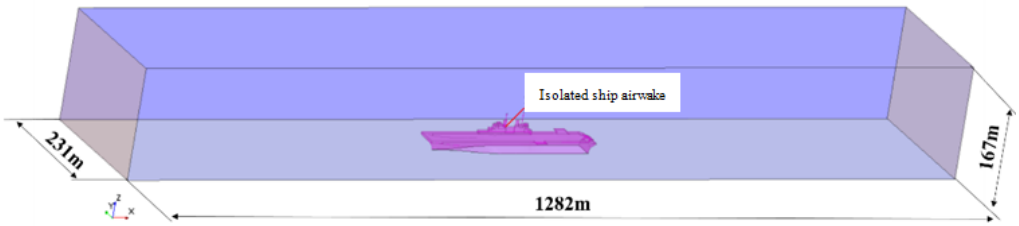

Figure 9-Main Scale of Computational Domain

Source: Author

This paper will use the trim mesh to improve calculation accuracy, and the ship deck surface, island, extended deck, bow, stern and other areas are partially refined, while the area around the ship is refined twice and three times, as shown in Figure 10.The total number of mesh refinement is 9.3 million.

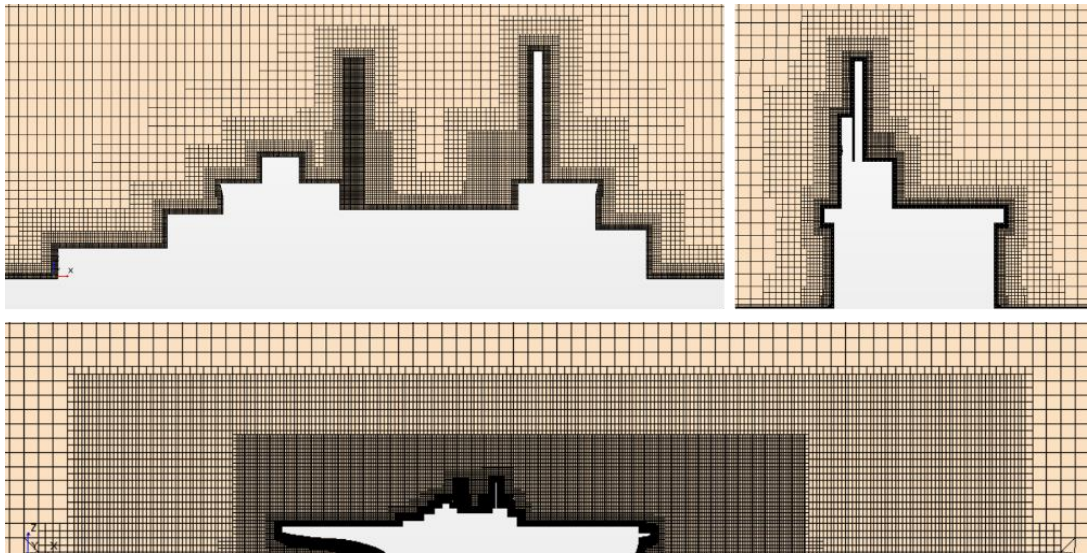

Figure 10-Computational Domain Grid

Source: Author

3.2.3 Calculation settings and boundary conditions

By comparing and analyzing the advantages, disadvantages and applicable ranges of each turbulence model and discrete method in Chapter 2, the calculation settings and boundary conditions for numerical simulation of isolated ship's airflow are shown in Table 7.

Table 7-Calculation Settings and Boundary Conditions

Turbulence numerical simulation method	RANS
Turbulence Model	RKE
Spatially discrete	First-order upwind scheme
Time Discrete	Implicit unsteady scheme
Boundary conditions	No sliding grid (hull) Sliding grid (water surface)

Boundary layer treatment	All y+ Wall Treatment
Physical properties	Uncompressible air

Source: Author

3.3 Example verification of scale model for calculation method

3.3.1 Example Description

Next is to verify the accuracy of the calculation method based on the PIV experimental data of the VSHAIP project of NASA AMES Research Center by Rajagopalan et al. (2005). The test was conducted in a 7 x 10 foot wind tunnel with a maximum wind speed of 350 feet per second. Figure 11 is a 1:48 LHA scaling mode for the test.

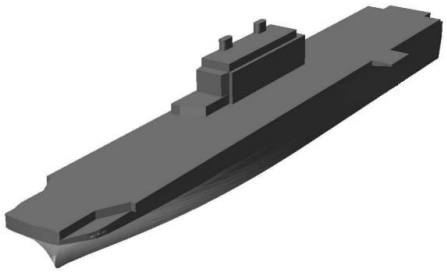

(a) 1:48 LHA physical model in wind tunnel (b) scaling mode

Figure 11-1:48 LHA physical and scale calculation model

Source: Author

Table 8 gives the dimension parameters of the full-size ship and the scaling model.

Table 8-Verify Model Size Parameters

Dimensional Parameters	Full-Size LHA Ship	1:48 Scale Model
Flight deck length	820ft	205.0in
Flight deck width	118.1ft	29.53in
Distance between waterplane and flight deck	64.5ft	16.13in

Source: Author

Several take-off and landing points are arranges on the deck of the scaling model.

The specific position of each starting point is shown in Figure 12. PIV test data of take-off and landing points 5 and 6 cannot be obtained due to the obstruction of test instrument structure.

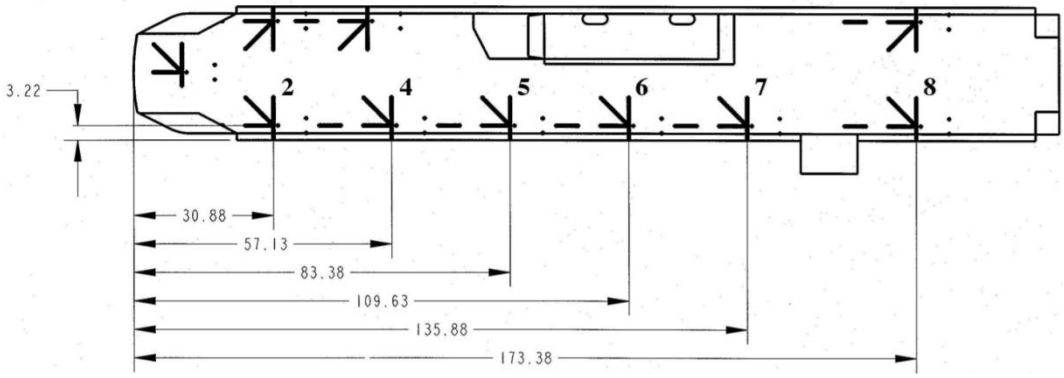

Figure 12-Arrangement of Starting and Descending Points in Inches for Compression Models

Source: Author

3.3.2 Calculation results

According to the data in Rajagopalan's paper, the PIV test results were compared with the calculation results in this paper from the four lateral monitoring lines 0.1322324 m above the deck with 0 degree wind direction angle and 22.5 ft/s=6.858 m/s wind speed above the take-off and landing points of 2, 4, 7 and 8 respectively, as shown in Figure 13, where V_z is the vertical velocity value of monitoring point and V_B is the inlet velocity value.

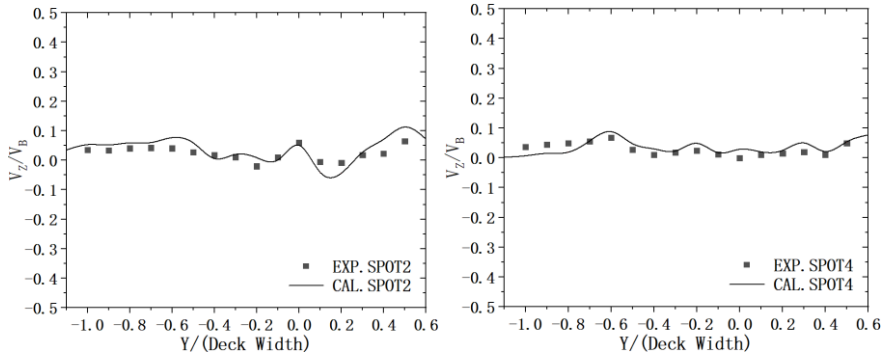

(a) Take-off and landing point 2 (b) Take-off and landing point 4

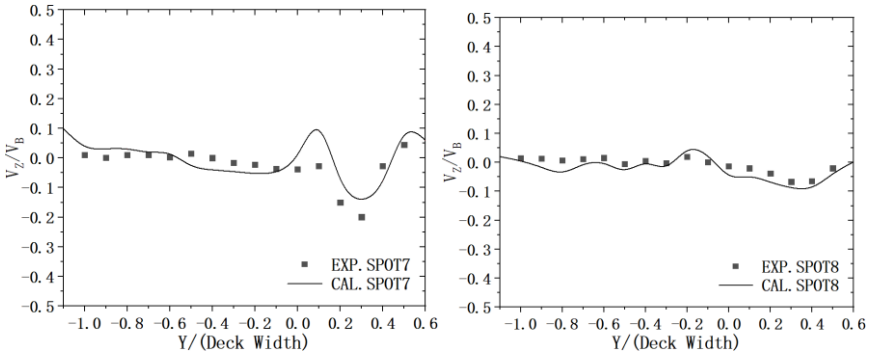

(c) Take-off and landing point 7 (d) Take-off and landing point 8

Figure 13-Monitoring results of take-off and landing points

Source: Author

From Figure 13, the maximum number of errors appears on the right side of point 7. In addition, the right part of point 2 also has a major error. However, the two large errors are far from the takeoff and landing point, which are out of consideration in the calculation of this paper. Generally speaking, although the calculated values are not identical with the test, the trend is basically consistent with the PIV test. The prediction of landing point and its left side is more accurate, which is just the key area of the real scale ship airflow studied in this paper. Therefore, the calculation and simulation method of the isolated ship in this paper are reliable for the prediction of the mainly investigated local flow field area.

3.4 Analysis of the influence of wind speed on the real scale ship's airflow

The precondition of boundary layer separation is that the wall and viscosity block the flow, and an inverse pressure gradient region existes.

From Figure 8, the area above the seven take-off and landing points keeps a certain distance from the hull. Therefore, if the flow field of each point is of Reynolds number independence, only one wind speed needs to be calculated for the same wind direction angle, and other wind speeds can be obtained by scaling, which will greatly reduce the amount of calculation and save cost.

On the vertical section of each point, 25 straight-line continuous monitoring points are set from bow to stern at 2m, 7m, 12m and 17m above the deck respectively. At the wind direction angle of 15 degrees on starboard side, obtain the dimensionless number of the speed of the monitoring point in the wind conditions of 5m / s, 10m / s, 20m / s and 30m / s respectively at the inlet, and the results are shown in Figure 14, where V is the combined speed value of each monitoring point, and VB is the inlet speed value.

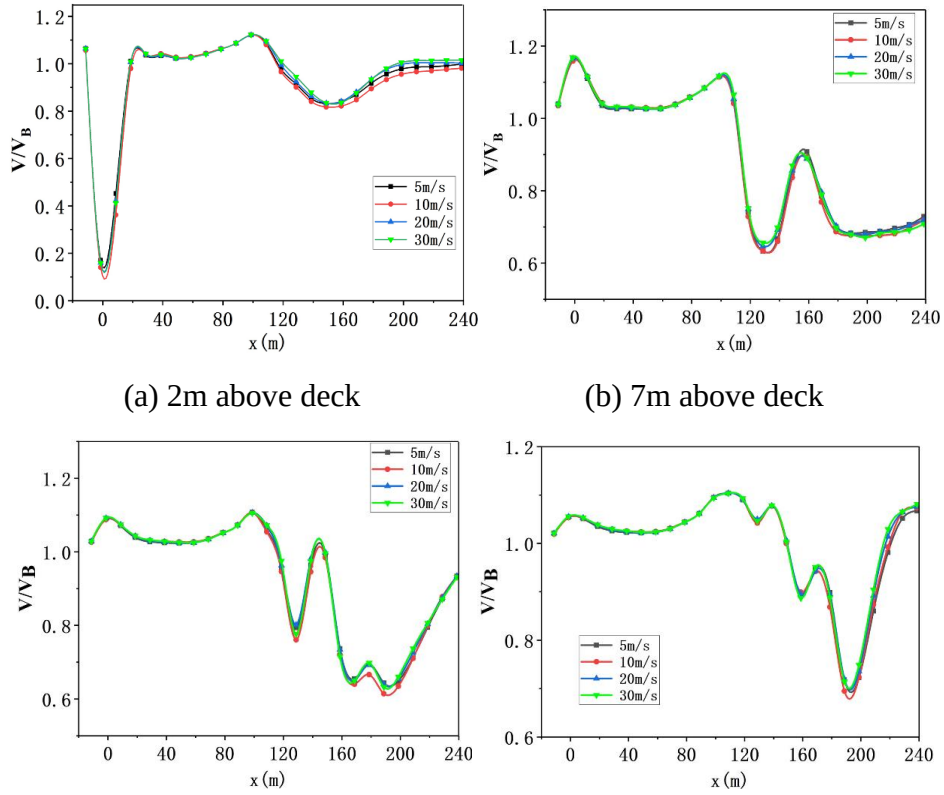

(a) 2m above deck (b) 7m above deck

(c) 12mabove deck (d) 17m above deck

Figure 14-Dimensionless results of each monitoring point under different wind speeds

Source: Author

From Figure 14, from 5m / s to 30m / s, the changing curve of speed dimensionless results of the monitoring points at different heights of the airflow around the takeoff and landing points with coordinates almost coincide, and the speed dimensionless

values at different wind speeds at each monitoring point are also very close. Therefore, it can be considered that in the range of 5m / s to 30m / s, for the flow field above the takeoff and landing point, the Reynolds number is independent.

At the same time, the velocity nephogram of horizontal section flow field at 5m and 15m above the deck is given, as shown in Figure 15 and Figure 16. Compared the velocity nephogram, it can be found that the velocity distribution of the same section is similar under different wind speeds. It should also be noted that the ratio of the maximum velocity is similar with the ratio of the inlet wind speed in the same set of nephogram, The relationships between the maximum velocity in the same set of cloud images are shown as follow:

$$\frac{24.795}{6.1901}=4.0056 \approx \frac{20}{5}=4\ ,\quad \frac{32.868}{8.2484}=3.9847 \approx \frac{20}{5}=4$$

This can further verify that in a certain range of wind speed, the velocity distribution of the ship's airflow is Reynolds number independent in most areas away from the wall.

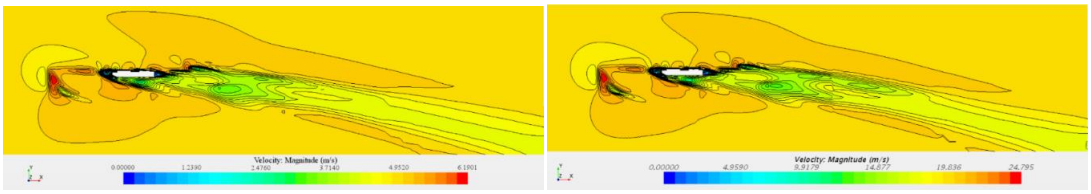

(a) 15 °starboard, 5m / s (b) 15 °starboard, 20m / s

Figure 15-Velocity nephogram of horizontal section at 5m above deck

Source: Author

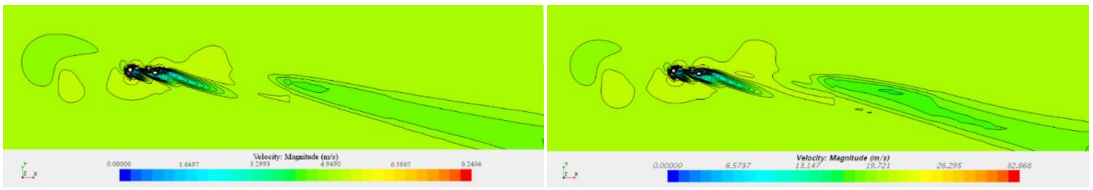

(c) 15 °starboard, 5m / s (d) 15 °starboard, 20m / s

Figure 16-Velocity nephogram of horizontal section at 15m above deck

Source: Author

It should be noted that the Reynolds number independence is only valid in a certain wind speed range. For the surface ship studied in this paper, the relative wind speed in actual navigation is generally below 30m/s. Even in the case of higher wind speed, the helicopter is not allowed to take off and land in this case. Also it is not necessary to study the very low wind speed (less than 5m/s).

Therefore, based on the analysis in this section, it can be considered that the ship's airflow, especially the region above the take-off and landing points concerned in this paper, is of Reynolds number independence.

3.5 Analysis of the influence of wind direction on the real scale ship's airflow

Under different wind directions, the ship air flow field has different structural characteristics. Based on the verification of Reynolds number independence, this section mainly analyzes the airflow around the hull with 10m / s wind speed, under 0 ° inflow, the port inflow (- 15 °, - 30 °, - 60 °, - 90 ° wind angle) and the starboard inflow (15 °, 30 °, 60 °, 90 ° wind angle), the key point is to analysis the development of vortices and speed distribution in different wind directions.

3.5.1 Vortex distribution under different wind directions

3.5.1.1 Positive front inflow

For the positive front inflow, i.e. 0 ° wind angle, the iso surfaces of vortex calcuated by λ2 and Q are shown in Figure 17.

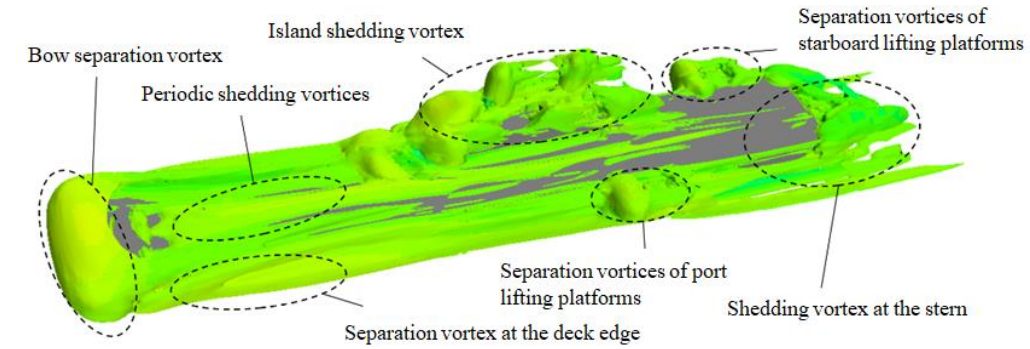

(a)λ2=0.02

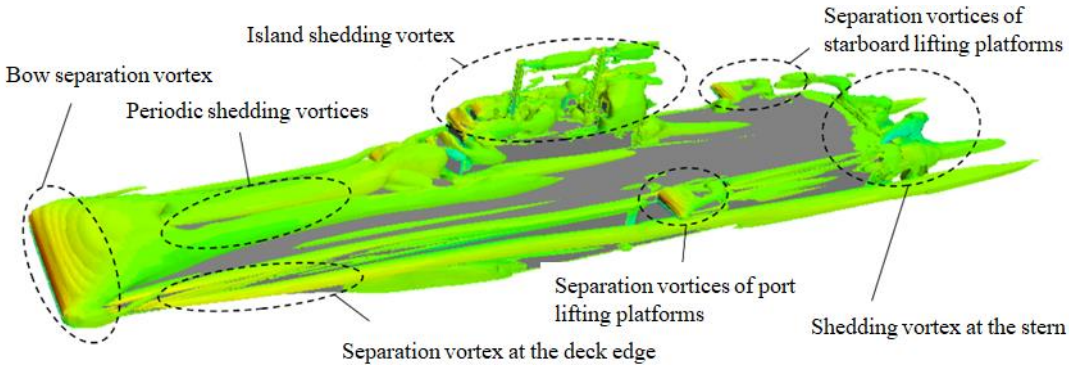

(b)Q=0.02

Figure 17-Iso-surface of vortex under positive front inflow

Source: Author

Combined with two figures, it can be seen clearly that there are six types of vortices in the ship's airflow under positive front inflow:

(1) The bow separation vortex, comes from the upwash separation due to the obstruction of front deck, as shown in Figure 18;

(2) The periodic shedding vortices are the trailing vortices formed by the bow separation vortices periodic fall back along the deck;

(3) The separation vortex at the deck edge, comes from the front inflow, blocked by the front edge of the deck, separated at the front hull to both sides while the upwash occurs, as shown in Figure 19. This is a pair of symmetrically rotating separated vortices.

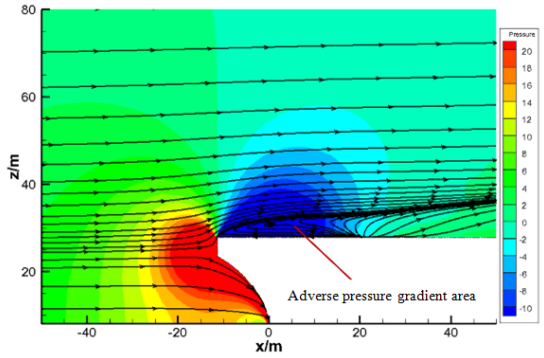

Figure 18-Flow separation at bow

Source: Author

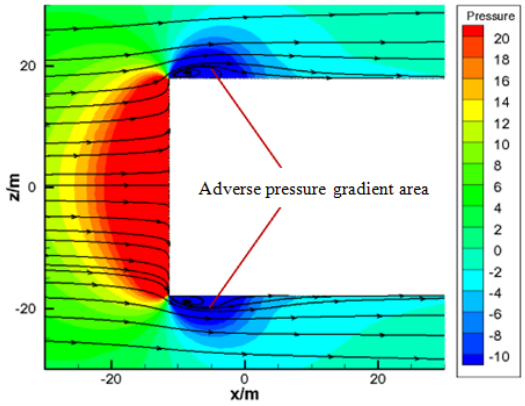

Figure 19-Flow separation at deck edge

Source: Author

(4) The island shedding vortex: because of island blocking, air flow separated and shedding at the back formed trailing vortex, as shown in Figure 20.

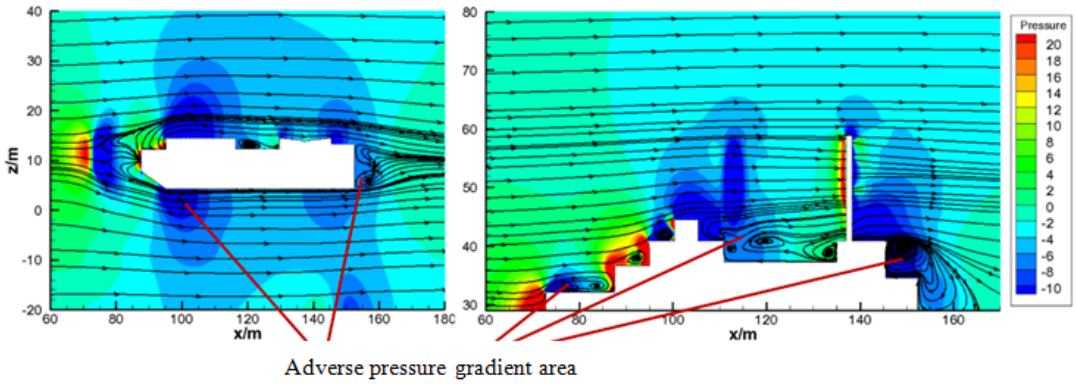

Figure 20-Flow separation caused by ship island

Source: Author

(5) The separation vortices of the port and starboard lifting platforms are similar to the bow separation vortices, they are formed by the upwash separation of the front inflow blocking by the leading edge of the lifting platform, as shown in Figure 21. This vortex may be mixed with the separated vortex at the deck edge.

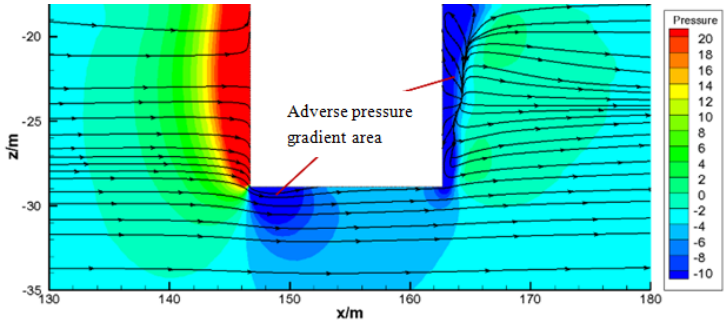

Figure 21-Flow separation caused by lifting platform

Source: Author

(6) The shedding vortex at the stern: when deck flow separated move along the reverse pressure gradient area at the stern, it separated and formed the shedding vortex, as shown in Figure 22.

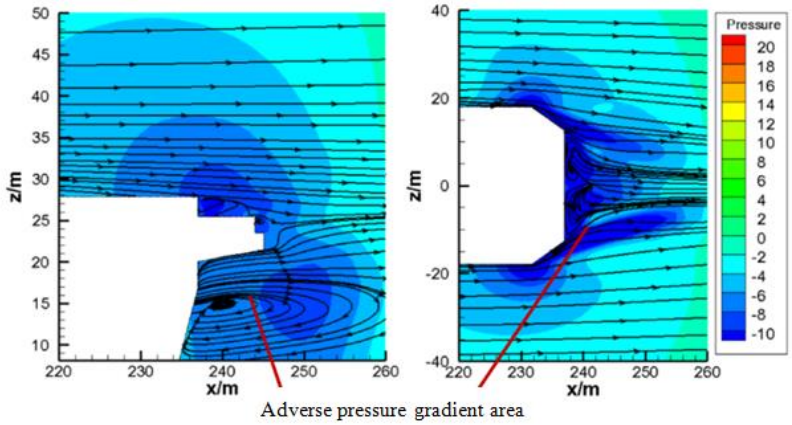

Figure 22-Flow separation at stern

Source: Author

Among them, the actual influence of the separation vortex of the port and starboard lifting platforms is relatively small, the effect on the airflow above the deck is relatively limited; the influence of the separation vortex of the stern is behind the

stern, and relatively low, mainly below the deck, far away from the take-off and landing path of the helicopter. Therefore, the first four types of vortices are the main reasons that affect the take-off and landing of helicopter.

According to the streamline and vertical velocity distribution of different section positions in Figure 23, the position distribution and influence range of vortex in the flow field can be analyzed more carefully.

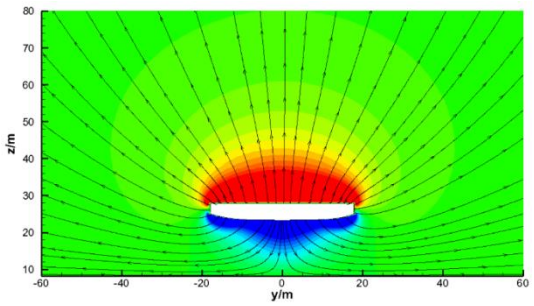

(a)x=-11m

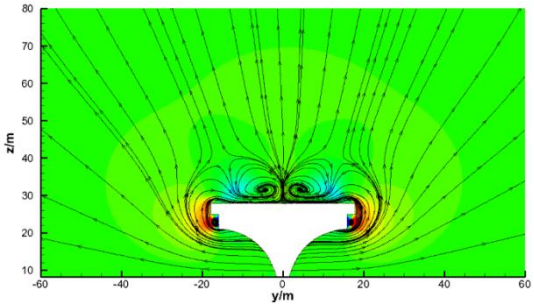

(b)x=20m(Point A)

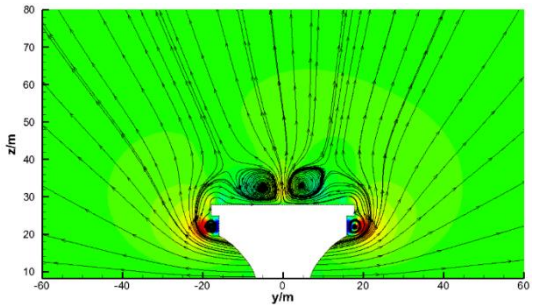

(c)x=51m(Point B)

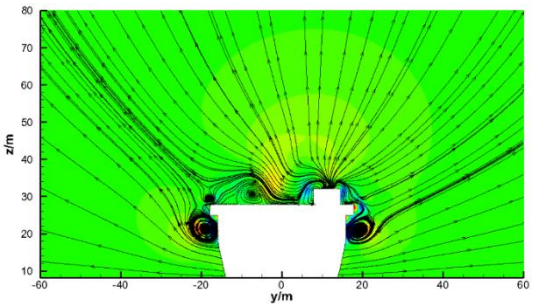

(d)x=82m(Point C)

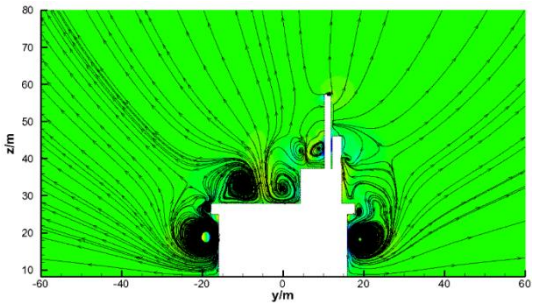

(e)x=113m(Point D)

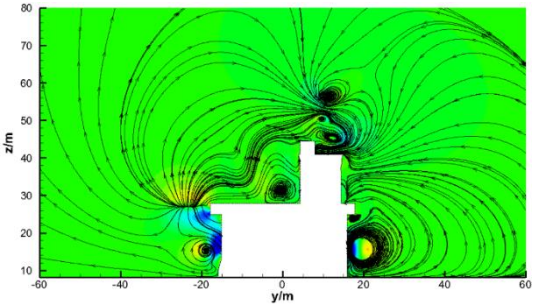

(f)x=144m

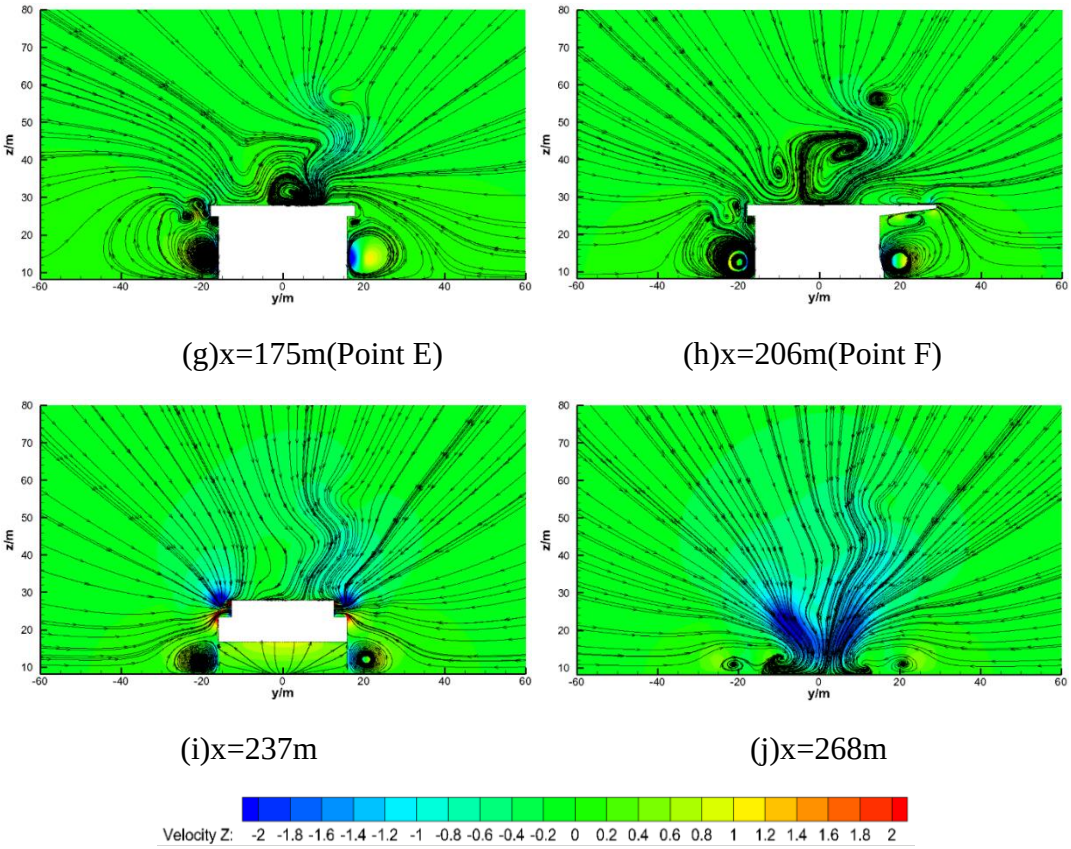

(g)x=175m(Point E) (h)x=206m(Point F)

(i)x=237m (j)x=268m

Figure 23-Streamline and vertical velocity distribution under front inflow

Source: Author

From Figure 23(a), the front inflow upwashed in front of the deck, and there are no other obvious vortices on this section.

From Figure 23(b) and Figure 20(c), a pair of distinct vortexes appears in the middle of the deck, which came from deck separation vortexes shedding backwards along the deck. The left one would create time-varying downwash flow over points A and B, which will influence the take-off and landing of the helicopters at these locations. It should also be noted that a pair of symmetrically rotating vortices, i.e. the separation vortices are formed on both sides of the ship below the edge, which are of high strength and may affect the helicopter at point B.

From the Figure 23(c), two pairs of distinct vortexes have been formed, which

develop backwards and influence each other at the same time.

In Figure 23(d), the airflow on the right is blocked by island and upwashed. Affected by the island, the left periodic shedding vortice became smaller and the right one disappeared. At the same time, the pair of deck edge separation vortices continues to develop backwards and become weaker.

From Figure 23(e), the intensity of the left periodic shedding vortices decreases while the range increases. An upwash flow is formed above point D. Due to the island, the air flow on the left separated and produced a weak separation vortex, interacts with one of periodic shedding vortex. At the same time, the pair of deck edge separation vortices continued to enlarge and became weaken.

In Figure 23(f), the left deck edge separation vortex weakens due to the separation of the port lifting platform. The left periodic shedding vortex has disappeared, while the separation vortices generated by the island continue to develop backwards. At the same time, the vortex street formed by the separation of mast over the island mixed with the upwash airflow became more complex.

In Figure 23(g), a strong and complex vortex structure formed behind the island because of the inverse pressure gradient region, but its influence only limited on the right side of deck. Also, a series of small vortexes appeared, with little influence on the helicopter. In general, point E has relatively small influence from the vortex and can be considered as an ideal take-off and landing point.

However, at point F, the influence of vortexes behind the island increases, caused a large range of vortexes gradually appears above point F, would form tumbling moment for the rotor and possibly pose a threat.

From Figure 23(i) to Figure 23(j), the ship airflow continues to develop backwards, with downwash flow coming from the stern. The separation vortices at the deck edge gradually weaken until they disappear behind the stern.

3.5.1.2 Port inflow

Vortex equivalents at different wind angles of port inflow are shown in Figure 24. From the figure, as the angle of port inflow increased, the influence of the bow separation vortex decreased and is been blown away from the deck after 60 degree wind angle on the port side.

As the wind direction angle increased, the ship airflow is gradually controlled by the upwash vortices at the left edge of the deck. The upwash vortexes generated on the left side of the deck are blown to the other side and violently collide with the island, resulting in intense flow separation around the island. However, most of the strong and complex vortices behind the island are outside the deck, which has a very limited influence on the take-off and landing points on the left side. The upwash vortices on the left side of the deck have a great influence on the airflow at the take-off and landing points.

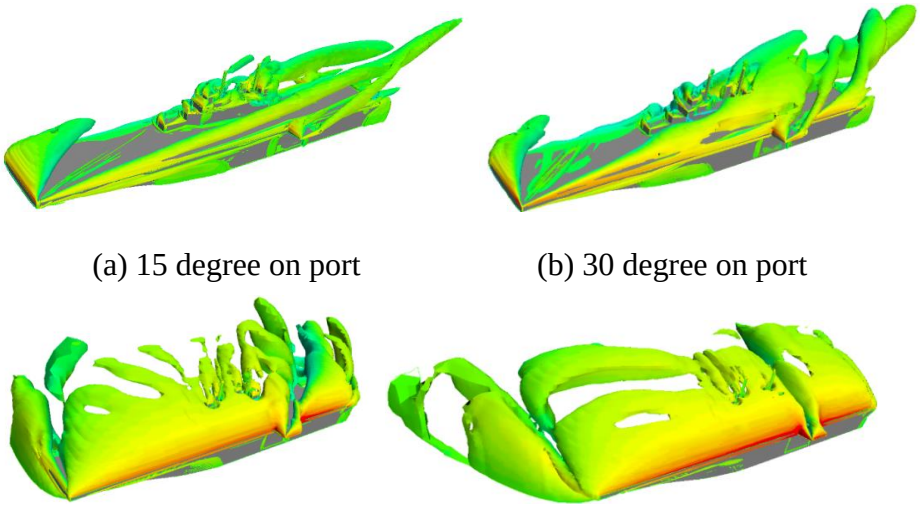

(a) 15 degree on port (b) 30 degree on port

(c) 60 degree on port (d) 90 degree on port

Figure 24-Vortex Iso-surface under Port Inflow (Q=0.02)

Source: Author

Taking the 30 degree on port as an example, the influence of vortex on ship airflow is analyzed in detail according to the streamline and vertical velocity distribution in

each section of Figure 25.

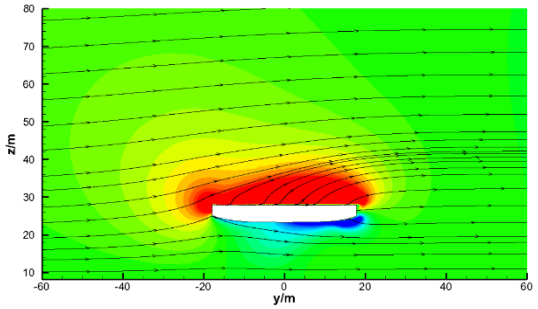

(a)x=-11m

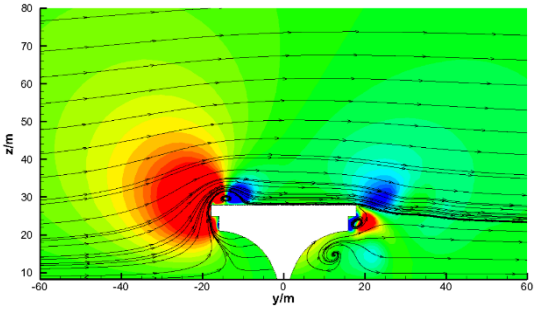

(b)x=20m(Point A)

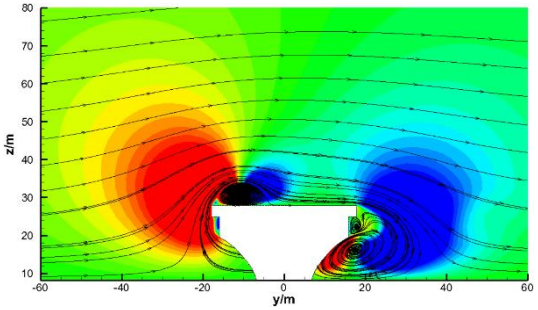

(c)x=51m(Point B)

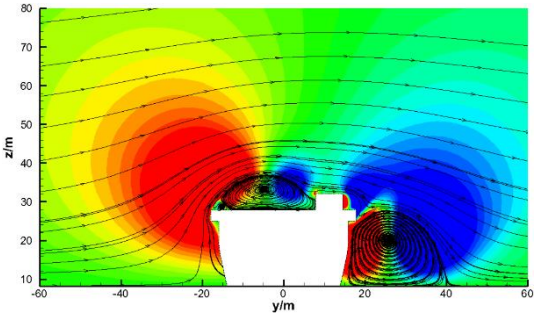

(d)x=82m(Point C)

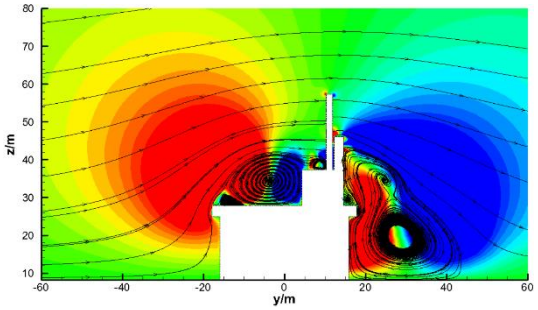

(e)x=113m(Point D)

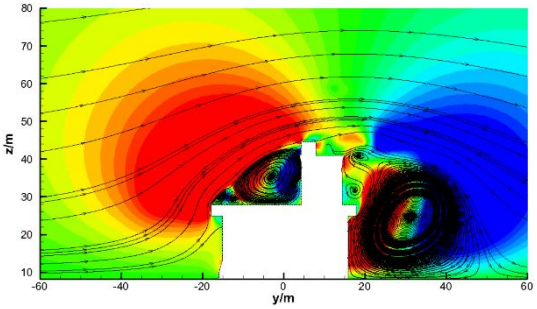

(f)x=144m

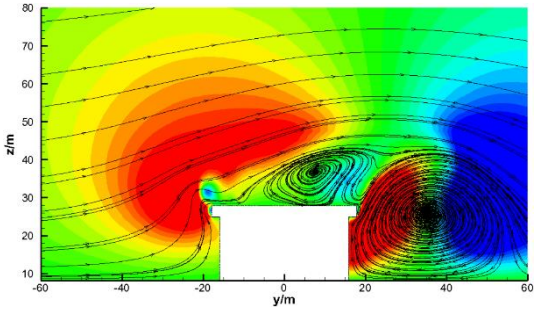

(g)x=175m(Point E)

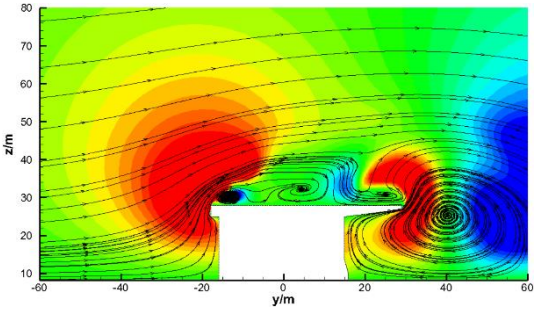

(h)x=206m(Point F)

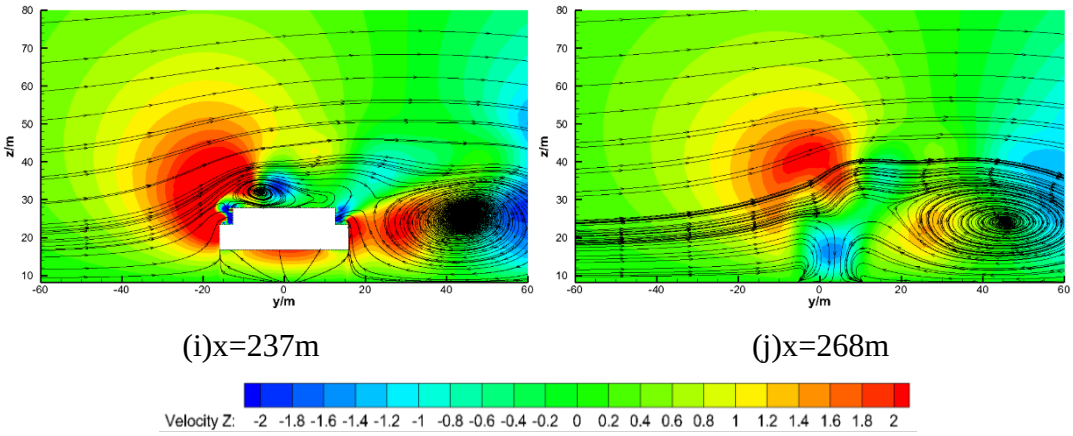

(i)x=237m (j)x=268m

Figure 25-Streamline and vertical velocity distribution under 30 degree on port

Source: Author

It can be seen from Figure 25(a) and Figure 22(b), there is no obvious vortex from the front edge to point A. However, there is a strong upwash flow on the left side, which would affect all take-off and landing points.

Starting from Figure 25(c), a small clockwise rotating vortex is formed on the left side. This vortex will generate downwash airflow within a certain height range on the right of point B. At the same time, there is strong upwash airflow on the left side of the point B. These two airflows will have a significant impact on the helicopter take-off and landing. Also, a clockwise rotating vortex is generated below the right deck. From Figure 25(d) to Figure 25(f), the influence of these two vortices gradually increases, but the right vortex is kept out of the right deck edge, which has no direct effect on the take-off and landing points. While the left vortex continued to increase and gradually spread to the middle of the deck, it eventually blocked by the island. The influence of the upwash airflow on the left is also increased, which made the take-off and landing more dangerous.

At Figure 25(g), the island is no longer blocking the airflow. Most of the left side vortexes deviated to the right. At this time, besides the right ones, vortices' scale increase, reaching 30 to 40 meters, but still not influencing the deck. Also, the

upwash airflow with over 2m/s vertical velocity on the left side of the deck covered most of the upper deck space. It can be said that the airflow near the point E becomes relatively stable and less affected by vortices.

Starting from the position of Figure 25(g) to Figure 25(j), the original left and right vortices gradually disappear and a weaker small vortex is generated. Eventually, all these vortices will disappear in the ship's wake flow field. Relatively speaking, the point F is also ideal at this wind angle.

3.5.1.3 Starboard inflow

Vortex equivalents at different wind angles of starboard inflow are shown in Figure 26. As can be seen from the figures, similar to port inflow, with increasing starboard inflow angle, the influence of the bow separation flow becomes smaller and smaller. Starting from the 60 degree on starboard, the bow separation flow is almost blown off the deck area. At this time, strong flow separation occurs at the right rear side of the island, generated a series of huge and complex vortices. Most of the upper deck area is controlled by island tailing vortices and deck right edge separation vortices.

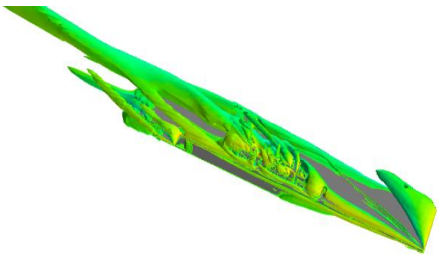

(a) 15 degrees on starboard

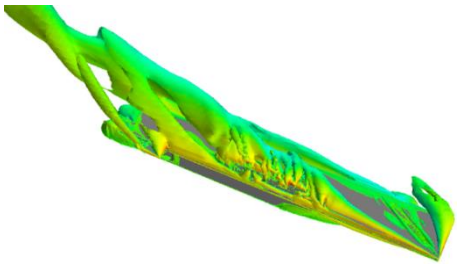

(b) 30 degrees on starboard

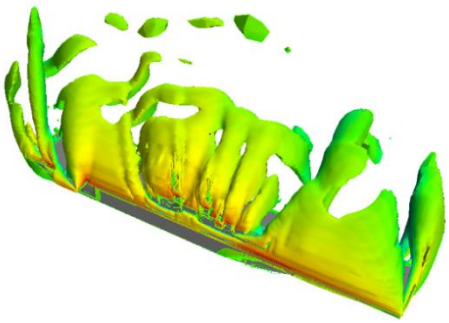

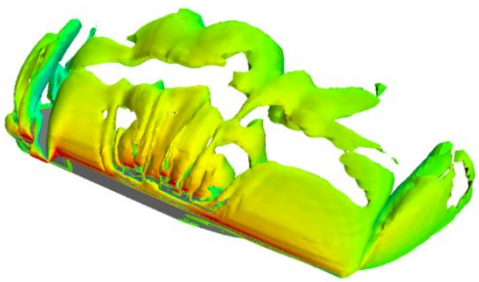

(c) 60 degrees on starboard (d) 90 degrees on starboard

Figure 26-Vortex Iso-surface under Starboard Inflow (Q=0.02)

Source: Author

Taking the 30 degree on starboard as an example, the influence of vortex on ship airflow is analyzed in detail according to the streamline and vertical velocity distribution in each section of Figure 27.

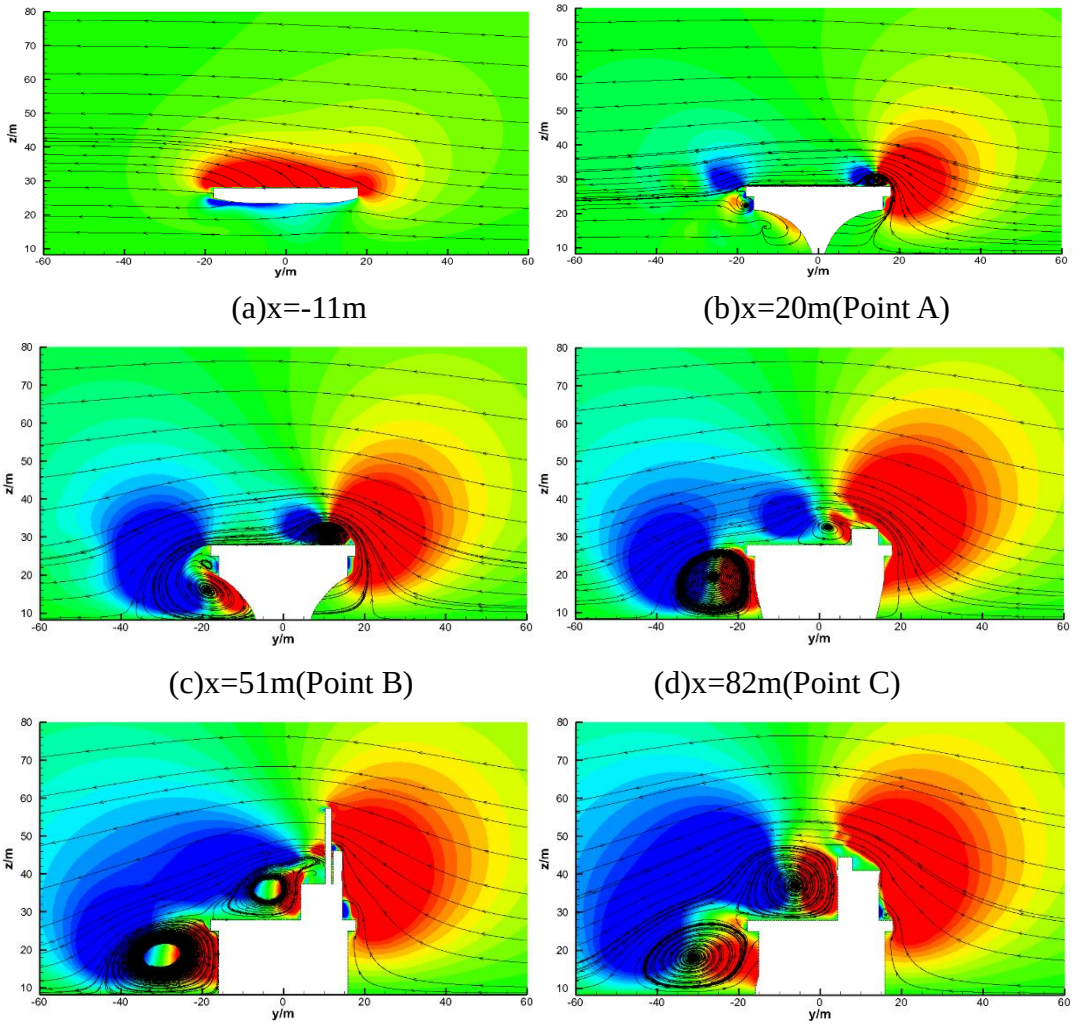

(a)x=-11m (b)x=20m(Point A)

(c)x=51m(Point B) (d)x=82m(Point C)

(e)x=113m(Point D) (f)x=144m

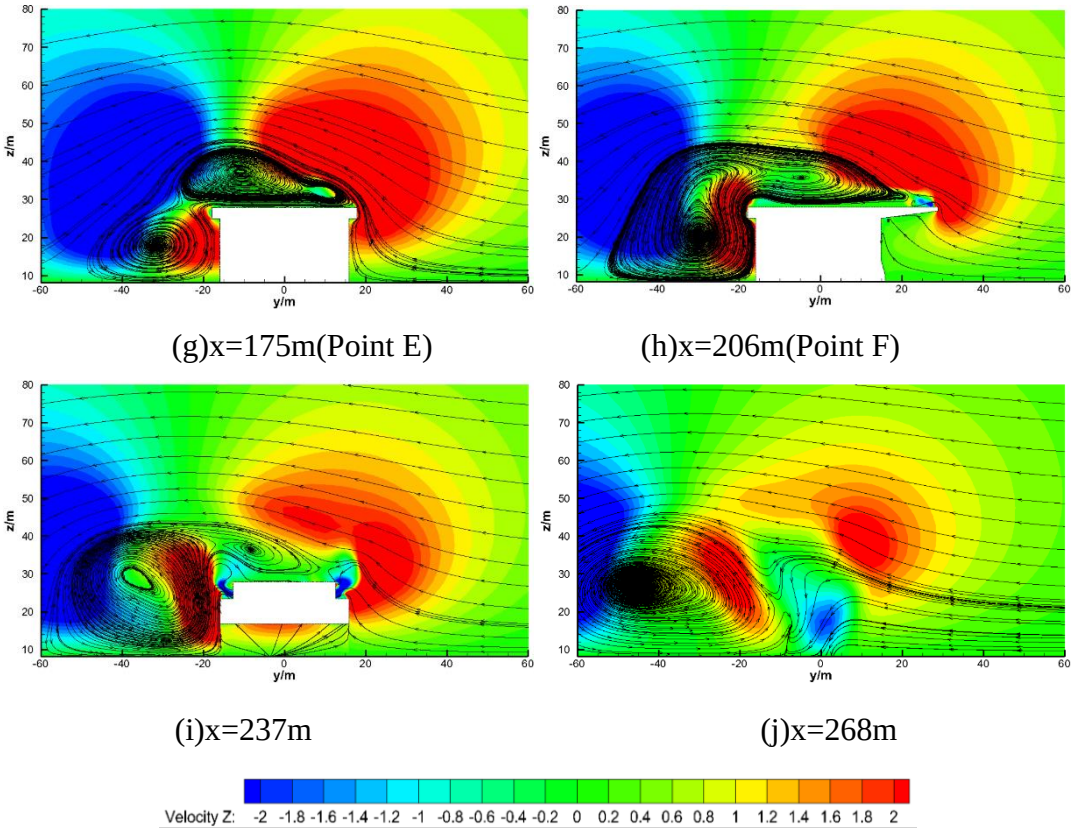

(g)x=175m(Point E) (h)x=206m(Point F)

(i)x=237m (j)x=268m

Figure 27-Streamline and vertical velocity distribution under 30 degree on starboard

Source: Author

In Figure 27(a) and Figure 27(b), as the hull in front of the island is completely symmetrical, it is similar to the 30 degree port inflow that there are no obvious vortex above the deck, but a strong upwash flow on the right at the point A. However, from point A to D, unlike port inflows, the upwash flow has no direct influences on the take-off and landing. Relatively speaking, point A is an ideal landing point.

Starting from Figure 27(c), an upwash vortex is generated above the right side of the deck and a downwash vortex is generated below deck. At the same time, the range and speed of downwash flow are significantly larger than those at point A. This downwash flow field with a wind speed more than 2 m/s will affect all the landing points backwards.

From Figure 27(d) to Figure 27(f), the right upwash vortices generated in Figure 27(c)

disappear because of the island; it also separated airflow and created a new strong separation vortex behind it. This vortex generates upwash flow on the left side and spreads downwash flow to the middle of the deck. From Figure 27(e) to Figure 27(g), the separation vortices extended, so point D and E may be affected simultaneously by time-varying and very unstable upwash and downwash airflows, as well as the vertical shear in the swirl airflow. Especially for point E, at 30 degree starboard inflow, the surrounding airflow becomes very unfriendly for take-off and landing.

On the location of Figure 27(h), the island separation vortices continue to spread to the left until they combine with the downstream vortices and form a large deformed vortex. This vortex, with a width of 50 meters, covers the entire deck surface and had negative effects on point F.

Until the positions of Figure 27(i) and Figure 27(j), this large deformed vortex gradually blown off the deck and eventually disappeared in the ship's wake flow field.

3.5.2 Velocity distribution under different wind directions

In addition to vortices, the vertical velocity distribution above the ship take-off and landing points also has a great influence on the safety of helicopters. It is necessary to analyze the vertical velocity distribution above the take-off and landing points of isolated ships in different wind directions.

Taking the AH-1 Cobra Attack Helicopter as an example, its rotor outer diameter is 13.4 meters, the height is 4.1 meters, and the center of the propeller after landing is about 4 meters above the deck. Therefore, height range from 4 m to 19 m above the landing points should be focused. The results are shown in Figure 28. In the picture, V_Z is the vertical wind speed, V_B is the inlet wind speed, and H is the height above the deck. For easy comparison, port inflow is marked in blue, starboard inflow in red and front inflow in black.

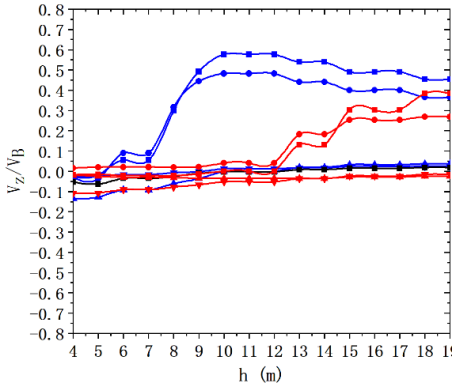

(a)Take-off and Landing Point A

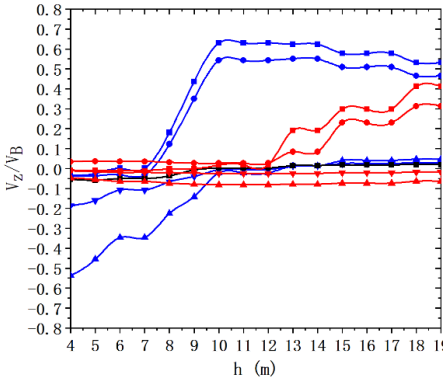

(b) Take-off and Landing Point B

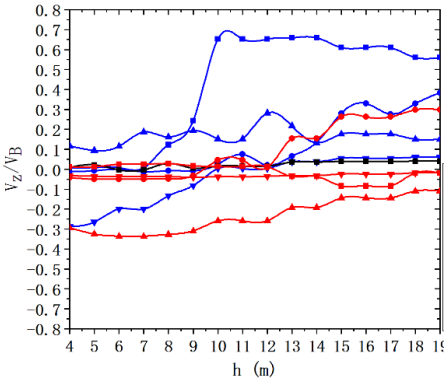

(c) Take-off and Landing Point C

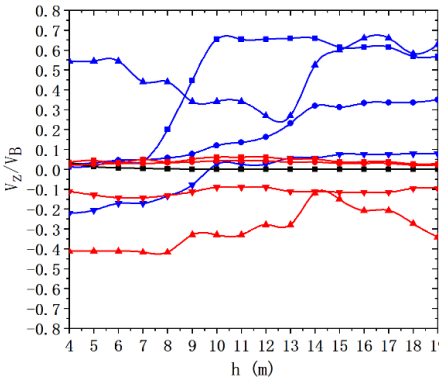

(d) Take-off and Landing Point D

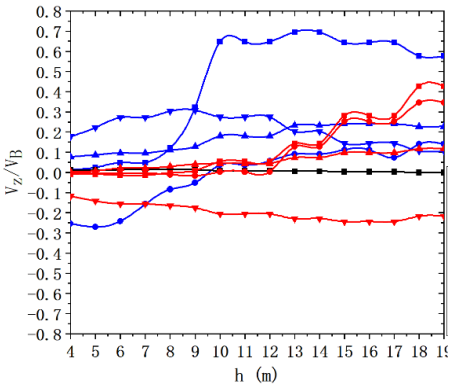

(e) Take-off and Landing Point E

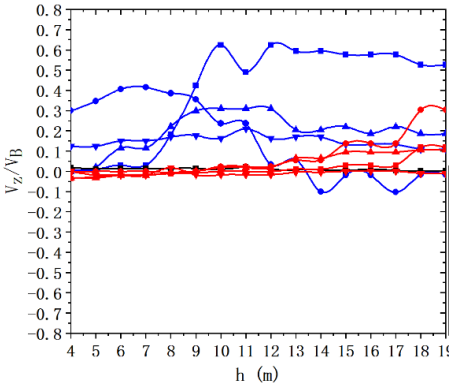

(f) Take-off and Landing Point F

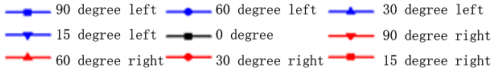

Figure 28-Vertical velocity distribution under different wind direction

Source: Author

Based on the results of Figure 28, points A and B are taken as examples for detailed

analysis.

From Figure 28(a), for Point A, the change of port inflow angle has more significant influence on the velocity distribution than that of starboard. When the starboard inflow angle increases above 60 degrees, more intense upwash flow appeared at about 8-11 meters above point A, the speed of upwash flow reaches the maximum value. As higher it goes, the speed of upwash flow slowly decreases. When the port inflow angle increases above 60 degrees, there will appear an upwash airflow growing 13 meters above point A. The speed of the upwash flow varies dramatically under 60-90 port inflow, 7 to 10 meters above the deck, which may pose a greater threat to the safety of the helicopter.

Compared with point A, the biggest difference for point B is that when the wind direction is 15-30 degrees port, 4-9 meters above the deck, downwash flow increases while height decreasing over point B. This downwash airflow will cause the helicopter being "sucked" towards the hull during the landing, which is extremely unfavorable for the helicopter operation. For other directions, the velocity distribution above the point B is similar to that of point A, that is in the range of 60-90 degrees port and starboard, strong upwash airflow will appear and influence operation.

In general, the influence of the port inflow angle change on the velocity distribution is more obvious than that of the starboard. Because each point analyzed in this paper is located on the left side, the port inflow would cause upwash airflow, making it easier for downwash flow appear above landing points; while the starboard inflow washed down after passing through the hull, causing downwash airflow above some landing points. However, at a certain height and port inflow angle, such as below 10m from deck, points B 30 degree port flow, points C and D 14 degree port flow, downwash airflow increase with decreasing height. In these cases, downwash airflow

is dangerous for helicopter landing operations, measures should be taken. Also, downwash airflow usually doesn't appear at the points A and F in all direction.

It should be noted that for point E, when the wind angle is 0 and 30 degrees to the right, the vertical speed above it is very low or slightly upwashed, but when the wind angle is within 15 degrees to the right, there is an obvious downwash flow above the point E, which shows the "inconsistency" of the vertical velocity distribution due to the continuous variation of the wind direction. This particular phenomenon can be explained with Figure 29.

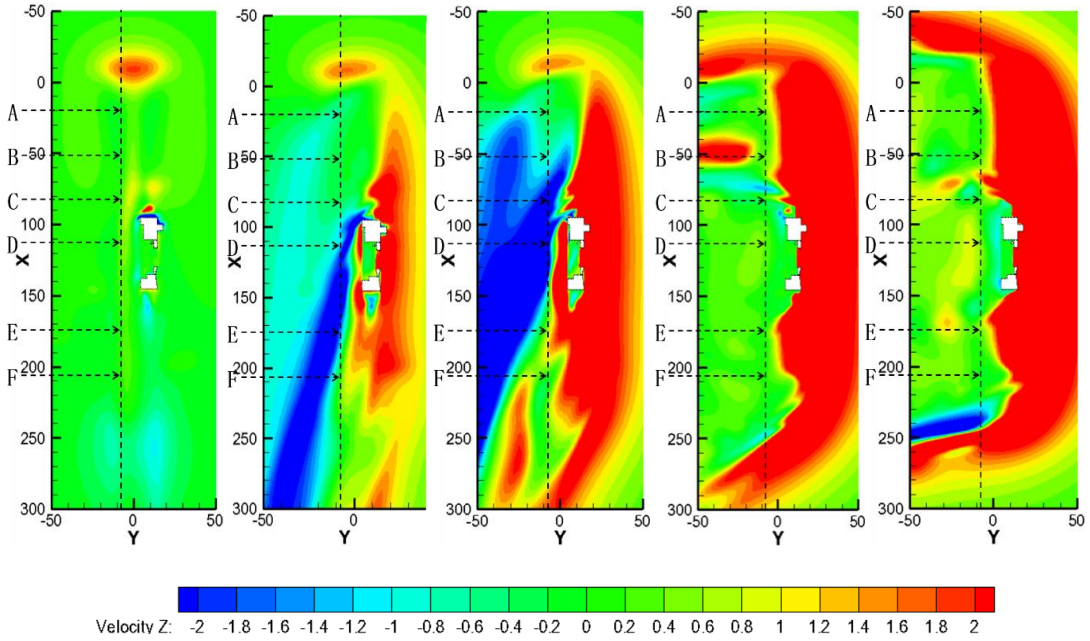

Figure 29-Vertical Velocity Nephogram of Horizontal Section at Different Wind Direction on Starboard (h=10m)

Source: Author

From Figure 29, when the inflow is 0 degrees, except for the upwash flow at the bow and the downwash flow at the stern, the vertical wind speed in most areas is close to 0; when the inflow is 15 degrees on starboard, point E is within the range of the island tailing flow, and point D is also affected, while the point F just missed the downwash area; when the wind is 30 degrees of starboard, points C and D are in the

downwash airflow zone, while the point E is outside. That is the existence of island creates a "discontinuity" in the velocity distribution.

The stable angle range above each point is shown in Table 9.

Table 9- Vertical Velocity Safe Wind Angle Range at Different Points

Take-off and Landing Point	Relative stable angle range for vertical speed
Point A	30 degrees port to 30 degrees starboard
Point B	0 degrees to degrees starboard
Point C	15 degrees port to 15 degrees starboard, near 90 degrees of starboard
Point D	15 degrees port to 15 degrees starboard, near 90 degrees of starboard
Point E	Near 0 degree, 30 degrees starboard
Point F	15 to 30 degrees starboard, near 90 degrees of starboard

Source: Author

3.6 Analysis of Different Landing Paths

3.6.1 Landing Path and Monitoring Point Setting

Taking the AH-1 Cobra Attack Helicopter as an example, its rotor outer diameter is 13.4 meters, the height is 4.1 meters, and the center of the propeller after landing is about 4 meters above the deck. The take-off and landing path of the helicopter from the 15 meters above the deck can be simplified into four types: vertical landing, side-to-side landing, side-to-rear landing and rear landing, as shown in Figure 30.

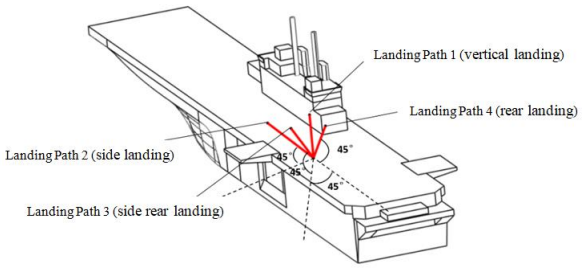

Figure 30-Landing Path Diagram

Source: Author

Taking Landing Path 1 as an example, the center of the rotor is O, and at the front, rear, left, right and center positions of rotor passing area (the circular section area with diameter of 13.4 m, 19 m to 4 m from rotor to deck), set up five monitoring lines F, B, L, R and O, extract the vertical wind speed data on the five lines, as shown in Figure 31.

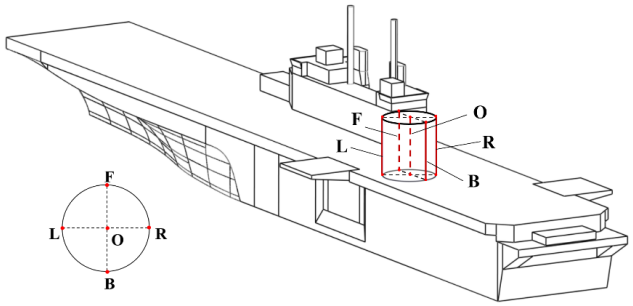

Figure 31-Relative position of flow field probe on landing path

Source: Author

3.6.2 Compare of Landing Paths

The following analysis is based on point A, where the wind speed is 10m/s front inflow. Under this condition, the vertical velocity distribution along the four landing paths is shown in Figure 32.

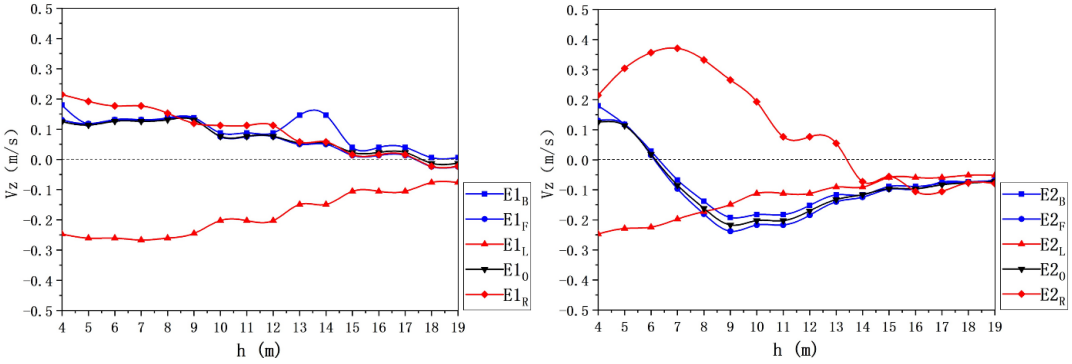

(a) Landing Path 1 (b) Landing Path 2

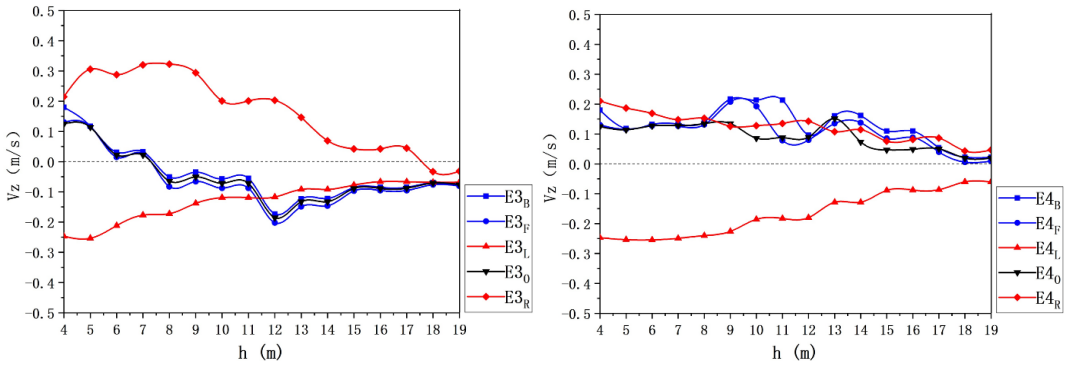

(c) Landing Path 3 (d) Landing Path 4

Figure 32-Vertical velocity distribution of each landing path at the point A with 10 m/s front inflow

Source: Author

In Figure 32, the monitoring lines F and B is marked in red, the larger the difference is, the larger the rotor pitch moment that may cause; lines L and R is marked in blue, the larger the difference is, the greater the rotor roll moment that may cause; "$E1_B$" represents the data obtained by Probe B in path 1, point E.

In general, the point A vertical airflow in each path is relatively weak under this wind condition, and the helicopter rotor roll moment may be greater than the rotor pitch moment. Relatively speaking, the vertical velocity changes of landing path 1 and 4 are relatively gentle, and there is no alternating upwash and downwash airflow on the same line. The velocity difference between the left and right is smaller than that of the other two. Therefore, from the vertical velocity distribution alone, the landing paths 1 and 4 are better than 2 and 3.

3.7 Summary

Based on the accuracy of the calculation method verified by a scaled model, this chapter calculates and analyses the structural characteristics of real-scale isolated ship’s airflow under different wind conditions. The main conclusions include:

(1) For isolated ships, the velocity distribution in most areas is independent of

Reynolds number in 5m/s to 30m/s inflow. That is, only one wind speed calculation needs to be carried out under the same wind direction, other wind speeds data can be obtained by scaling, thus greatly reducing calculation workload.

(2) When under front inflow, the ship airflow mainly produces six types of vortexes: the bow separation vortex, the periodic shedding vortices, separation vortex at the deck edge, island shedding vortex, separation vortices of the port and starboard lifting platform, shedding vortex at the stern. The first four will significantly affect the take-off and landing operation.

(3) For front inflow, only in terms of vortices and vertical velocity distribution, the relatively ideal take-off and landing points are C and E; for 30 degree port side inflow, the relatively ideal points are A, E and F; for 30 degree starboard side inflow, the relatively ideal points are A and B.

(4) For the safety of take-off and landing, the front inflow is obviously better than port and starboard inflow; the influence of the wind direction changes on the velocity distribution is more obvious in the port direction than that in the starboard; when the starboard side comes in, the presence of the island will cause the continuous change of wind direction and the "discontinuity" of the vertical velocity distribution.

(5) Through the analysis of velocity distribution of different wind speed, the wind angle range with relatively stable vertical wind speed at each point is shown in Table 9.

(6) With 10m/s positive front inflow, the landing path 1and 4are ideally better than path 2 and path 3, in terms of vertical velocity distribution alone.

CHAPTER 4 NUMERICAL SIMULATION OF SHIP-HELICOPTER AIRFLOW

4.1 Introduction

The airflow of surface ship is a complex time-varying multi-factor coupling flow field; the relationship between factors is shown in Figure 33.

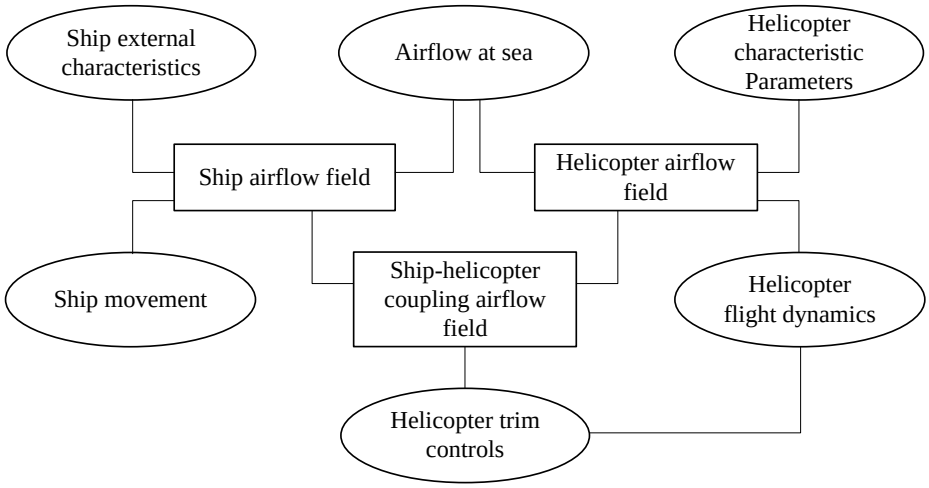

Figure 33-Coupling relationship of various factors in the problem of ship's air flow field

Source: Author

The third chapter studies the structural characteristics of isolated ship’s airflow, but when it comes to the theoretical wind operation envelope and the evaluation of multiple schemes for the ship design, it is not enough. It is necessary to consider the helicopter as the analysis object to carry out the numerical simulation of the ship-helicopter coupling airflow.

In order to realize the ship-helicopter coupling numerical simulation, this chapter proposes and compares three kinds of motion simulation grid schemes: overlapping-overlapping grid, overlapping-sliding grid, overlapping-virtual disk grid. The overlapping-virtual disk method is selected, and verified with ROBIN wing

body interference test. Then the ROBIN was enlarged and taken into coupling simulation.

4.2 Motion simulation grid for ship-helicopter coupling airflow

Compared with the entire ship airflow, the helicopter can be divided into three parts: rotor, fuselage and tail rotor. Because the simulation in this chapter is only a numerical example, not an engineering practice application, and the influence of the tail rotor is relatively weak compared with that of the rotor, the tail rotor will not be considered in this paper. At the same time, the numerical simulation of the coupling airflow is relatively complex, and based on the existing commercial softwares, this chapter will not consider the dynamic grid which requires higher grid quality.

In the following part several grid schemes that are suited for ship-helicopter coupling airflow simulation will be compared and explained.

4.2.1 Overlapping-overlapping grid

As shown in Figure 34, this method uses overlapping nested grids for the translation motion of helicopter fuselage and the rotation of the rotor.

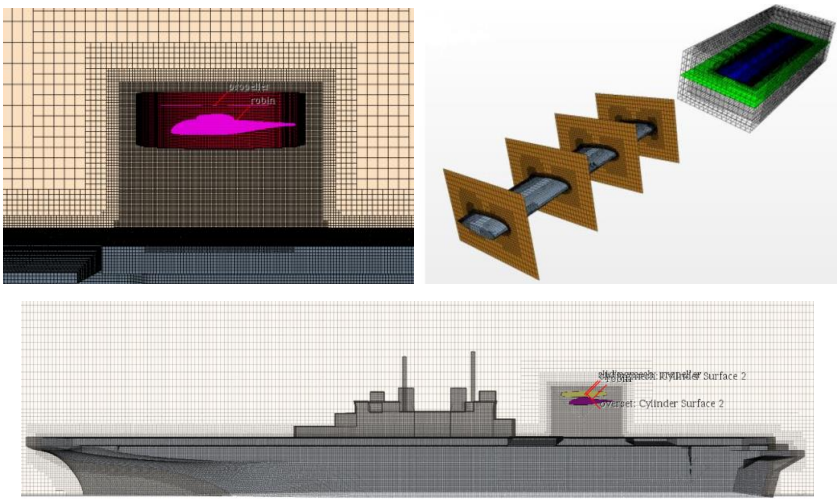

Figure 34-Overlapping-overlapping grid scheme

Source: Author

(1) Specific operation

The whole landing path is grid refined, and an overlapping grid is set for the entire helicopter, nested in the ship background grid. At the same time, the four blades are set with overlapping grid, nested in the helicopter grid.

(2) The motion obedience relationship between coordinate systems

The rotation of the blade in the local coordinate system is subject to the translation of the fuselage overall coordinate system.

(3) Correspondence of grid size

The dimension of the external interface 1 of the helicopter fuselage embedded grid should correspond to the partial refinement grid of landing path. The dimension of the external interface 2, 3, 4 and 5 of the blades embedded grid should correspond to the internal grid of the helicopter fuselage embedded grid.

(4) Calculation of time estimation

Under the overall background grid density of the ship is consistent with that of the isolated ship, the total grid of this scheme is 17 million. If the maximum linear speed of blade rotation is 200m / s, to ensure no problem for data exchange on the interface, the maximum time step can be estimated as 8×10^{-4}s, and the maximum number of internal iterations per time step is set to 5.

In order to complete the simulation of 10s helicopter landing, this paper used a 32-core computer with 2.5GHz CPU frequency for preliminary calculation attempt, found that it needs about 85 seconds for each iteration, then to finish the entire simulation would take $\frac{10}{8 \times 10^{-4}} \times 5 \times 85 = 5312500\text{s} \approx 1475\text{h}$.

Obviously, the calculation time is too long, which is not practical in engineering.

4.2.2 Overlapping-sliding grid

As shown in Figure 35, this method uses overlapping nested grids for translational

motion of the helicopter fuselage, sliding grids for the rotors. Compared with the overlapping-overlapping grid, the sliding grid is used to simulate the rotating motion of blades, which saves the overlapping grid number, and simplifies the whole grid refinement process.

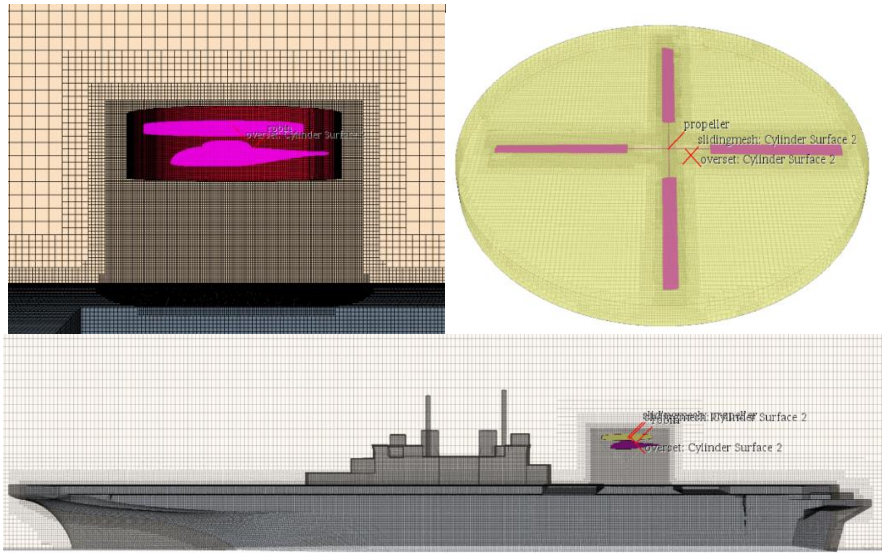

Figure 35-Overlapping grid sliding grid scheme

Source: Author

(1) Specific operation

The whole landing path of the helicopter is grid refined, and an overlapping grid is set for the entire helicopter, nested in the background grid of the ship. At the same time, set a sliding grid for the four blades, and the "filling" is in the reserved internal "cavity" obtained by the Boolean operation of the overlapping nesting area of the helicopter.

(2) The motion obedience relationship between coordinate systems

The rotation of the rotor in the local coordinate system is subject to the translation of the fuselage in the overall coordinate system.

(3) Correspondence of grid size

The dimension of the external interface 1 of the helicopter nested grid should be

corresponding to the local refinement grid of the landing path, and the interface 2 of the sliding grid of the "filled" rotor should be corresponding to the internal grid of the helicopter nested grid.

(4) Calculation of time estimation

Keeping the overall background grid density of the ship consistent with that of the isolated ship, the total grid of this scheme is 16 million. If the maximum linear speed of blade rotation is 200m / s, to ensure that there is no problem for data exchange on the interface, according to the mesh size, the estimated maximum time step is set to 8 × 10-4s, and the maximum number of internal iterations per time step is 5.

In order to complete a 10s landing simulation, this paper used a 32-core computer with a CPU frequency of 2.5GHz for preliminary calculation attempt, found that it needs about 60s for each iterative step calculation, then to finish the entire simulation would take $\frac{10}{8 \times 10^{-4}} \times 5 \times 60 = 3750000\text{s} \approx 1040\text{h}$.

Although the calculation time of this scheme is nearly 40% shorter than the previous one, the time is still too long to meet the actual needs.

4.2.3 Overlapping-virtual disk model

As shown in Figure 36, the scheme uses a virtual disk model to simulate the airflow of rotor, and the virtual disk and fuselage are embedded in the ship background grid with overlapping grid. The advantage is that the virtual disk model is used for the blade rotation, and the time step doesn't need to be as small as the sliding grid or overlapping grid, which would reduce time cost.

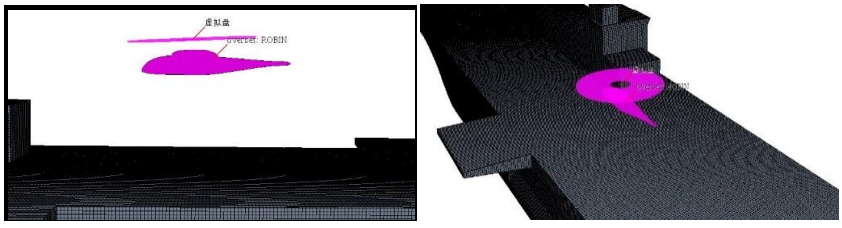

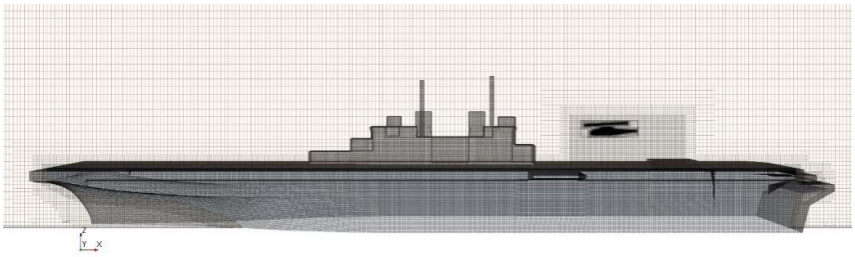

Figure 36-Overlapping-virtual disk model

Source: Author

(1) Specific operation

Set up the virtual disk model and locally refine it, also refine the whole landing path, set the helicopter as an overlapping grid, nested in the ship background grid.

(2) The motion obedience relationship between coordinate systems

The virtual disk coordinate system is subject to the translational motion of the fuselage overall coordinate system.

(3) Correspondence of grid size

The external interface 1 grid size of the fuselage nested grid should correspond to the local refinement grid size of the landing path.

(4) Calculation of time estimation

Keeping the overall background grid density of the ship consistent with that of the isolated ship, the total grid of this scheme is 14 million. The maximum time step is 5 × 10-3s, and the maximum number of internal iterations per time step is 5.

In order to complete a 10s landing simulation, this paper uses a 32-core computer with a CPU frequency of 2.5GHz for preliminary calculation attempt, found that it needs about 40s for each iterative step calculation, then to finish the entire simulation would take $\frac{10}{5\times10^{-3}}\times5\times40=400000\text{s}\approx111\text{h}$.

In fact, after the initial steady-state calculation of the convection field, the convergence will be accelerated, so the calculation time will be further shortened.

In general, choosing the overlapping-virtual disk model will reduce the calculation

time by 10 to 20 times compared with the other two schemes, which is of engineering practicability. However, the accuracy of using virtual disk model to simulate helicopter rotor needs further verification.

4.3 Example verification of wing body interference of virtual disk model

4.3.1 Example description

In order to verify the accuracy of using the virtual disk model to simulate the helicopter rotor based on the Robin wing body interference test conducted by NASA in Langley's 14 foot × 22 foot subsonic wind tunnel in 2000, the specific forward flight state of the Robin fuselage and virtual disk model is taken as example of verification.

Figure 37 shows the NASA's Robin wing body interference test device, Figure 38 shows the Robin fuselage and virtual disk model used in this paper. The scale of the two is exactly the same.

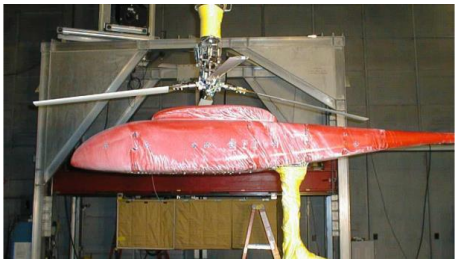

Figure 37-NASA's Robin wing body interference test device

Source: Author

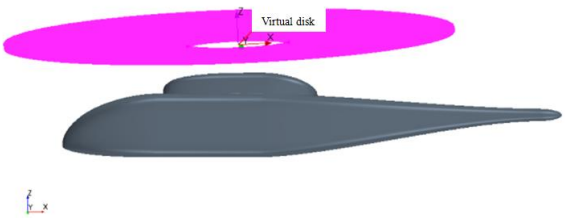

Figure 38-Robin fuselage and virtual disk calculation model

Source: Author

The specific parameters of this example are shown in Table 10.

Table 10-The specific parameters of rotor in forward flight state

Physical quantities	Value	Unit
Number of blades	4	—
Outer radius of rotor	0.860552	m
Undercut radius	0.207	m
Airfoil	NACA0012	—
Chord length b	0.066294	m
Disk thickness t	0.02	m
Rotor Solidity σ	0.098	—
Speed n	2000	rpm
Disk density ρ	1.176	Kg/m^3
Advance ratio μ	0.151	—
Disk angle of attack α_s	-3	deg
Transverse cyclic pitch A_1	-1.8	deg
Vertical cyclic pitch A_2	2.3	deg
Rotor collective pitch φ_0	7.7	deg

4.3.2 Calculation results

Figure 39 shows the pressure distribution of Robin wing body interference model, using the virtual disk model for rotors.

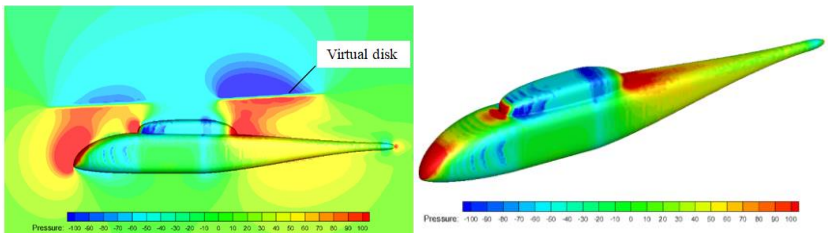

Figure 39-Pressure distribution of rotor body interference model simulated by virtual disk

Source: Author

In NASA's wing body interference test, multiple time average pressure monitoring

points and dynamic pressure monitoring points are set on the model surface, among which the time average tension monitoring points are arranged on the four cross section sidelines at the location $x/l = 0.35,1.17,1.35,1.54$, as shown in Figure 40. In the figure, l is half of the total fuselage length, l =39.35 in = 999.49mm; "○" indicates the time average pressure monitoring point, and "●" indicates the dynamic pressure monitoring point.

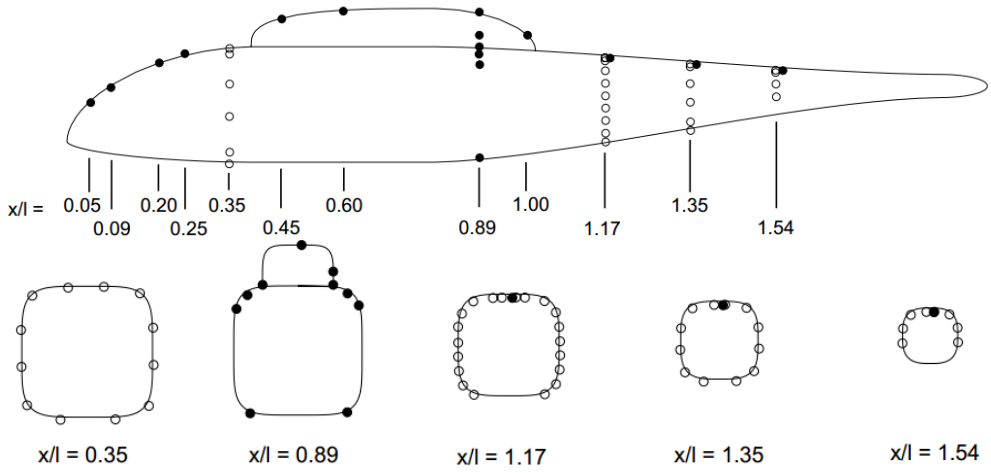

Figure 40-Layout of surface pressure monitoring points of NASA wing body interference model

Source: Author

This paper compares the time average pressure test data with the simulation results of the rotor virtual disk model, shown in Figure 41.

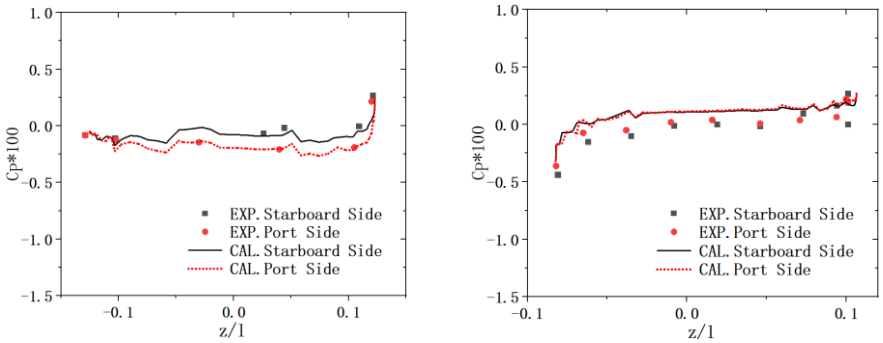

(a) x/l=0.35 (b) x/l=1.17

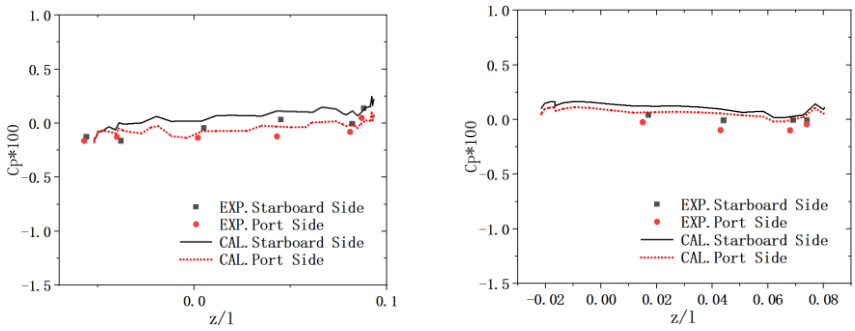

(c) x/l=1.35 (d) x/l=1.54

Figure 41-Comparison of time average pressure monitoring points interference model

Source: Author

The pressure coefficient C_P in the figure is determined by the following equation:

$$C_P \times \frac{2}{\mu^2} = \frac{P - P_\infty}{\frac{1}{2}\rho_\infty V_t^2 \frac{V_\infty^2}{V_t^2}} = \frac{P - P_\infty}{\frac{1}{2}\rho_\infty V_\infty^2}$$

It can be seen that, using the virtual disk to simulate the rotor wing body interference model, the results of the fuselage surface pressure obtained are different from the test: the calculation data at the front of the fuselage is well matched with the test, the rear data is higher than test. However, the results are consistent with the experimental data, and the error is acceptable, so it can be considered that the accuracy of using the virtual disk model to simulate the rotor and fuselage meets the requirements.

4.4 Numerical simulation of ship-helicopter coupling airflow

4.4.1 Example description

Based on the feasibility of using the virtual disk, point E is selected as the helicopter take-off and landing point of the coupling calculation, the front inflow speed is 10m/s. The helicopter model is assumed to land vertically at a constant speed of 1m/s from 8 meters above the deck. This part will takes this assumption as an example to

carry out the coupling calculation.

As the surface ship model calculation is of real scale, in order to meet the actual scale requirements, the Robin fuselage above is enlarged to 7.5 times of its original size, and the specific parameters of the rotor are also changed. The adjusted parameters are shown in Table 11.

Table 11-Adjusted rotor calculation parameters

Physical quantities	Value	Unit
Outer radius of rotor	6.45414	m
Undercut radius	1.5525	m
Chord length b	0.497205	m
Disk thickness t	0.15	m
Speed n	267	rpm
Advance ratio μ	0.0555	—

4.4.2 Comparative analysis before and after coupling

After the helicopter fuselage and rotor are coupled into the ship's airflow, at the initial state of calculation, height between the helicopter model's bottom and the deck is 8m, compare the local airflow characteristics of the landing area before and after the coupling.

4.4.2.1 Streamline and vortex distribution

The streamline and vortex distribution before and after coupling are shown in Figure 42 and Figure 43.

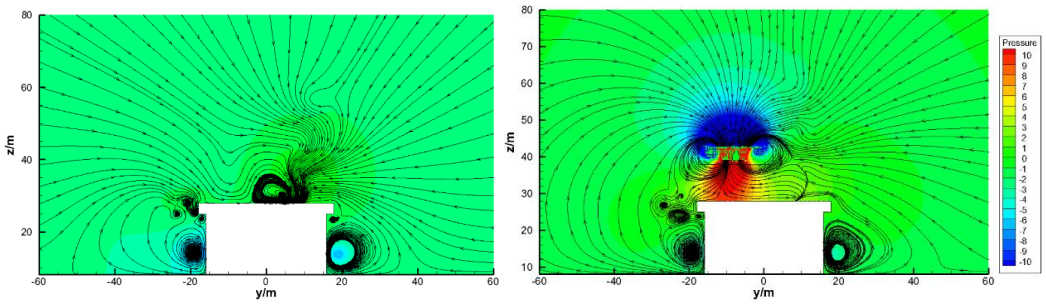

(a) Before coupling (b) After coupling

Figure 42-Streamline distribution of the same section (x = 174m) before and after coupling

Source: Author

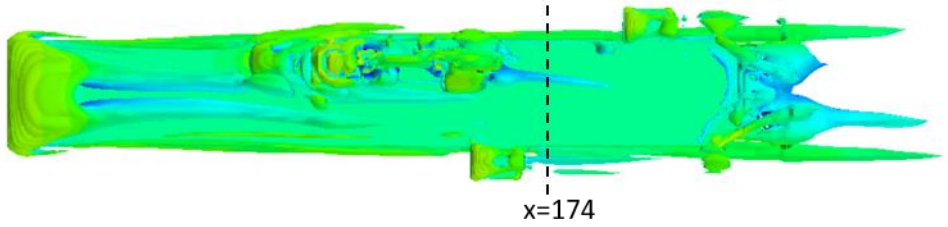

(a) Before coupling

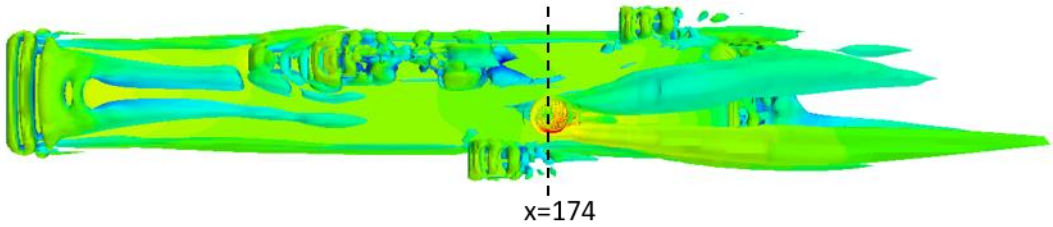

(b) After coupling

Figure 43-Vortex iso-surface before and after coupling (Q= 0.02)

Source: Author

As can be seen from Figure 42, after coupling, the downwash flow from rotor completely changes the streamline distribution above the deck, forming a new airflow environment. According to Figure 42 and Figure 43, the two ends of the coupled helicopter rotor generate a large range of circulation, resulting in a pair of incompletely symmetric vortices with opposite rotation direction. It can be predicted that when the helicopter takes off and lands at the point E in the figure, all the points behind E will be affected. Besides, due to the deck obstruction, the interaction between the downwash vortex and separation vortex at the deck edge is not obvious.

4.4.2.2 Surface pressure distribution of ship

Figure 44 shows the pressure distribution on the surface of some warships before and after coupling.

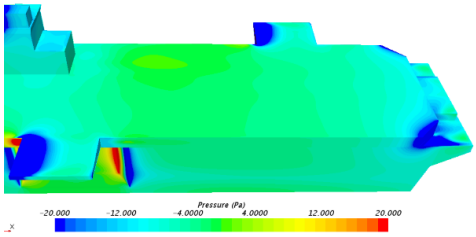

(a) Before coupling

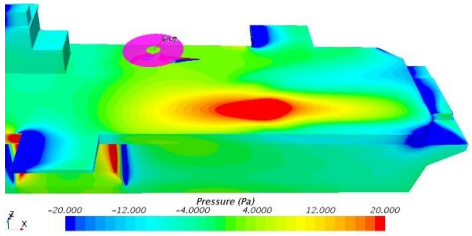

(b) After coupling

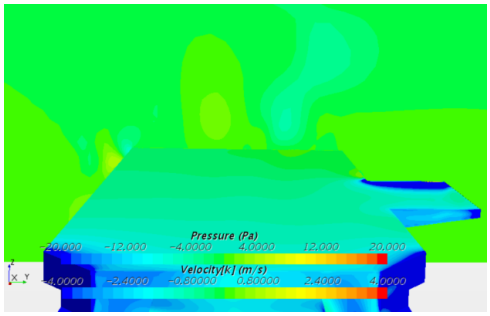

(c) Before coupling (cross section is colored according to vertical velocity distribution)

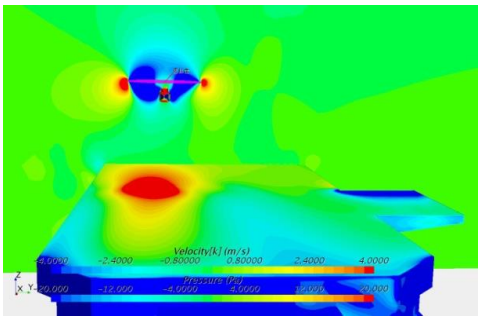

(d) After coupling (cross section is colored according to vertical velocity distribution)

Figure 44-Surface pressure distribution of the ship before and after coupling

Source: Author

From Figure 44(b) (d), it can be seen that, under the front inflow, the downwash flow from rotor impacts on deck and forming a local high pressure area.

4.4.2.3 Velocity distribution

Figure 45 and 49 show the vertical velocity distribution before and after coupling, 6m and 18m above the deck height.

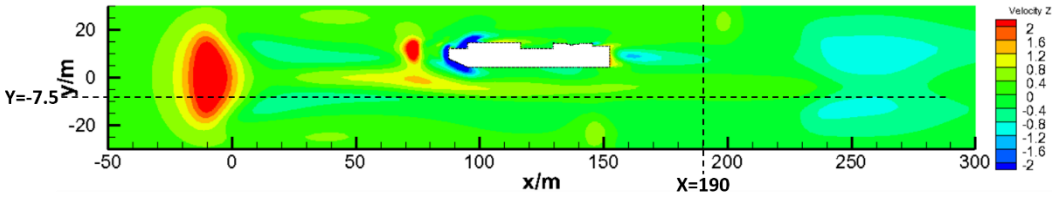

(a) Before coupling

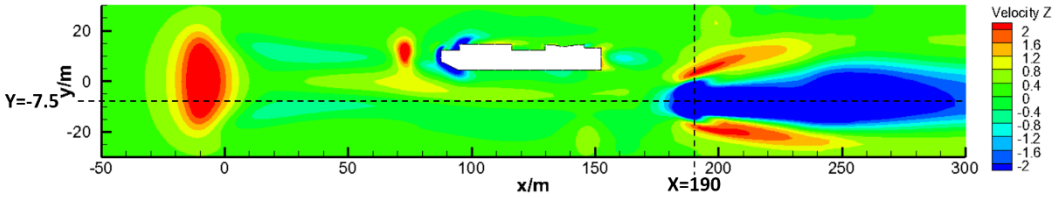

(b) After coupling

Figure 45-Vertical velocity distribution before and after coupling (H = 6m)

Source: Author

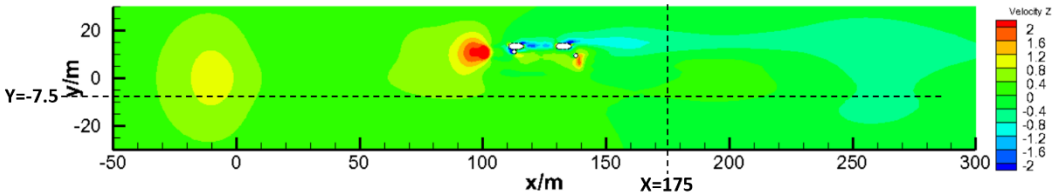

(a) Before coupling

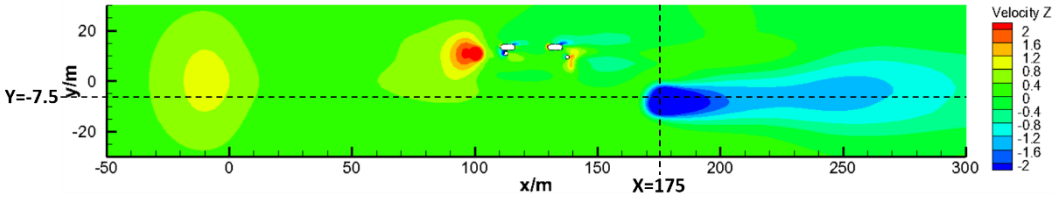

(b) After coupling

Figure 46-Vertical velocity distribution before and after coupling (H = 18m)

Source: Author

As shown in Figure 45 and Figure 46, for 6m above the deck, velocity data on two lines: y = -7.5m and x = 190m are taken, and for 18m above the deck, partial velocity data on: y = -7.5m and x = 175m are taken. These four lines' velocity distribution before and after coupling is shown in Figure 47-53:

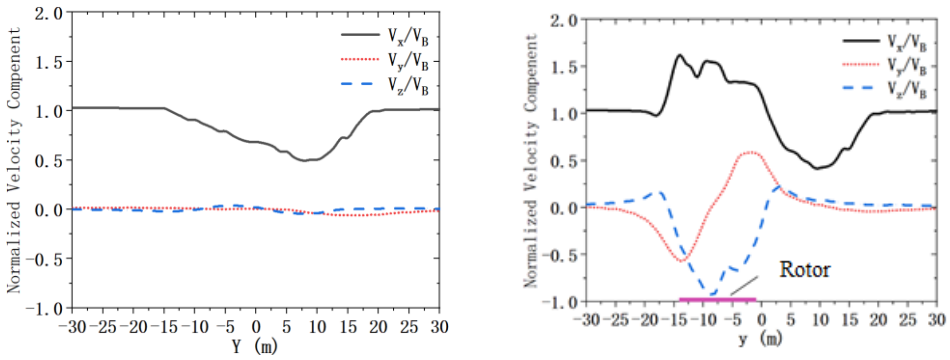

(a) Before coupling (b) After coupling

Figure 47-Velocity distribution on h=6m， X=190m

Source: Author

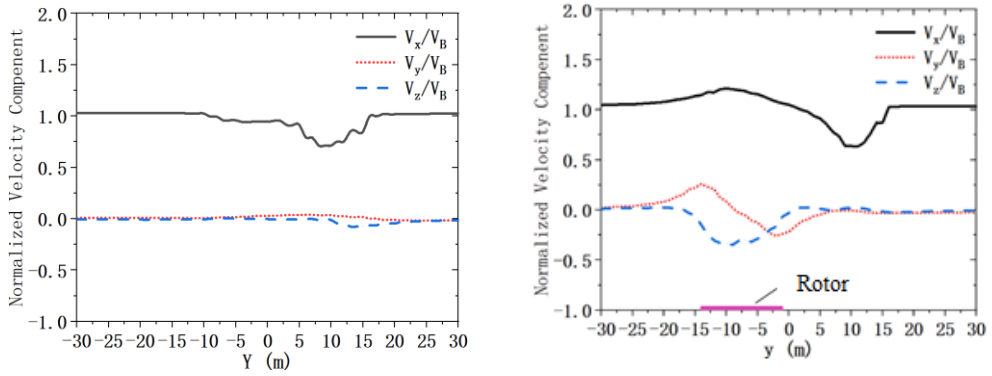

(a) Before coupling (b) After coupling

Figure 48-Velocity distribution on h=18m， X=175m

Source: Author

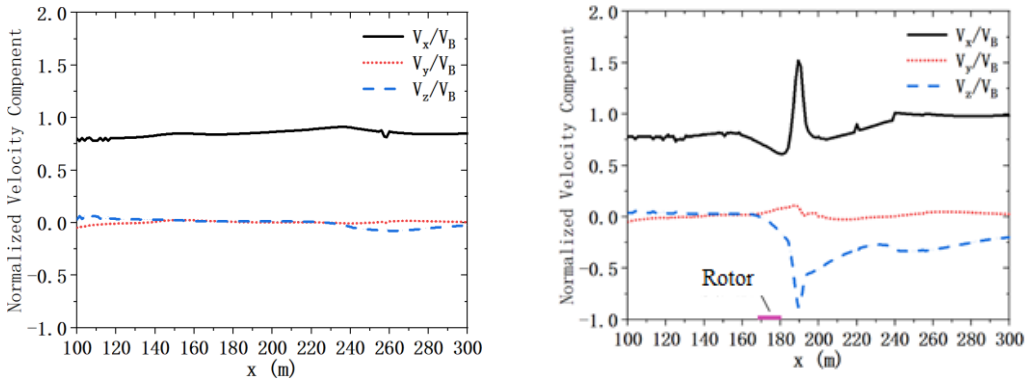

(a) Before coupling (b) After coupling

Figure 49-Velocity distribution on h=6m， Y=-7.5m

Source: Author

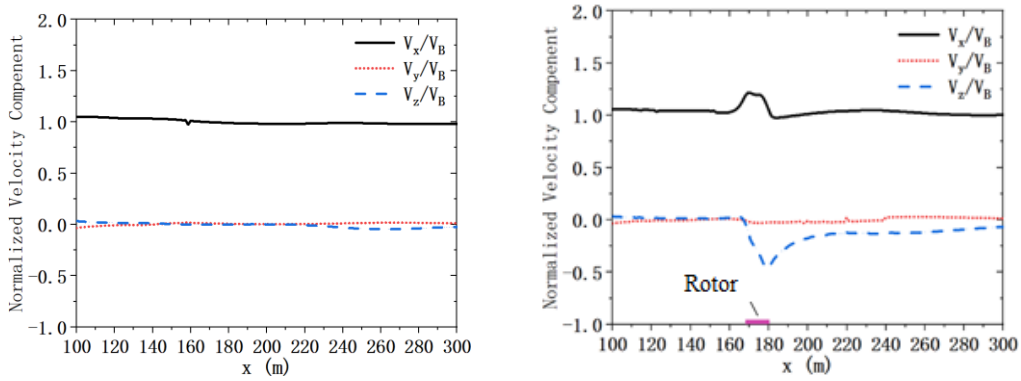

(a) Before coupling (b) After coupling

Figure 50-Velocity distribution on h=18m， Y=-7.5m

Source: Author

It can be seen that the velocity distribution changes significantly after coupling.

As shown in Figure 47, at the position of H = 6m, x = 190m, from the left end to the right end of the rotor disk, the velocity component V_x first increases, and then locally fluctuated and decreases lower than the inflow velocity. The increase of V_x is due to the acceleration effect of the longitudinal pitch angle of the rotor on the front inflow. The fluctuation of V_x comes from the undercutting of the rotor blade, and V_x reduced to below the incoming velocity is because it enters the tailing area of the island.

As shown in Figure 51, the straight line H = 6m, x = 190m passes through the lower part of the circulation area, causing the velocity component V_y fluctuate in the opposite direction. At the same time, the downwash flow from rotor causes a significant change in the vertical velocity component V_z, the maximum increasing amplitude is close to the income velocity.

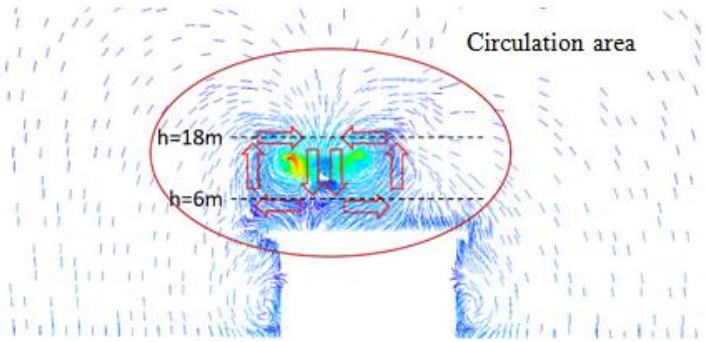

Figure 51-Circulation area above deck caused by rotor

Source: Author

In the same way, at the straight line of Figure 48, Figure 49 and Figure 50, the distribution of velocity components along the straight line also shows similar changes. In general, when the helicopter is coupled into the ship's airflow field, the velocity distribution near the takeoff and landing points and the rear is obviously changed by the rotor. Also, the influence of rotor on velocity distribution below the rotor is more obvious than that above.

4.4.3 Comparative analysis of coupling calculation and isolated superposition

As above, monitoring points are set on the four straight lines: X = 190m and y = -7.5m on H = 6m, and x = 175m and y = -7.5m on H = 18m. The vertical velocity distribution obtained from coupling is compared with simple superposition of the isolated ships and helicopter, in order to explain the necessity of coupling. The results are shown in Figure 52.

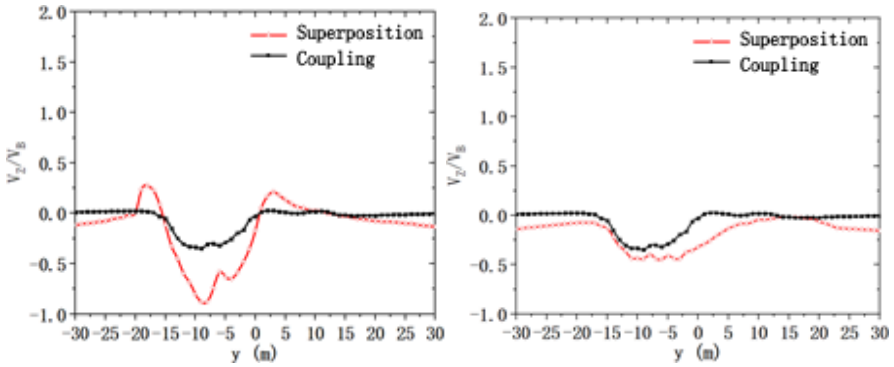

(a) h=6m，X=190m　　(b) h=18m，X=175m

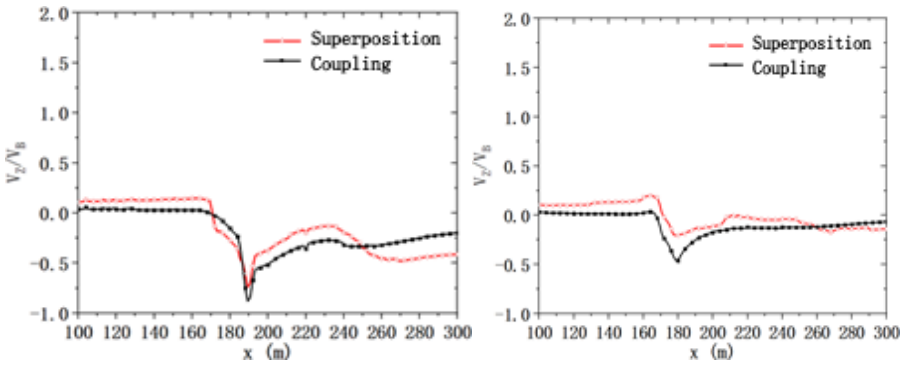

(c) h=6m，Y=-7.5m (d) h=18m，Y=-7.5m

Figure 52-Comparison of vertical velocity distribution from coupling calculation and isolated superposition

Source: Author

From Figure 52, the vertical velocity distribution difference between coupling and superposition is obvious. Especially at H = 6m and x = 190m, the maximum difference is more than 1.5 times of the coupling data. Moreover, data obtained from the isolated calculation is quite disorderly and unevenly distributed, which is inconsistent with the actual situation.

To a certain extent, this shows that the results obtained only by simple superposition are not reliable. Although in the previous, some useful conclusions have been obtained from that, but for further practical problems, it still need to be more accurate, such as the solution of the helicopter coupling aerodynamic force, the ship-helicopter coupling operation envelope, and the comparison and evaluation of the ship airflow scheme, it is necessary to simulate the ship-helicopter coupling airflow.

4.4.4 Flow field change during landing process

In this example, point E is selected as the helicopter take-off and landing point for coupling calculation. The front inflow speed is 10m/s. The helicopter model is assumed to land vertically on the deck at a constant speed of 1m/s from 8 meters

above.

The whole landing process takes 8 seconds, it is set to automatically extract the flow field information every second, and after process, the velocity nephogram and vortex change are shown in Figure 53-58.

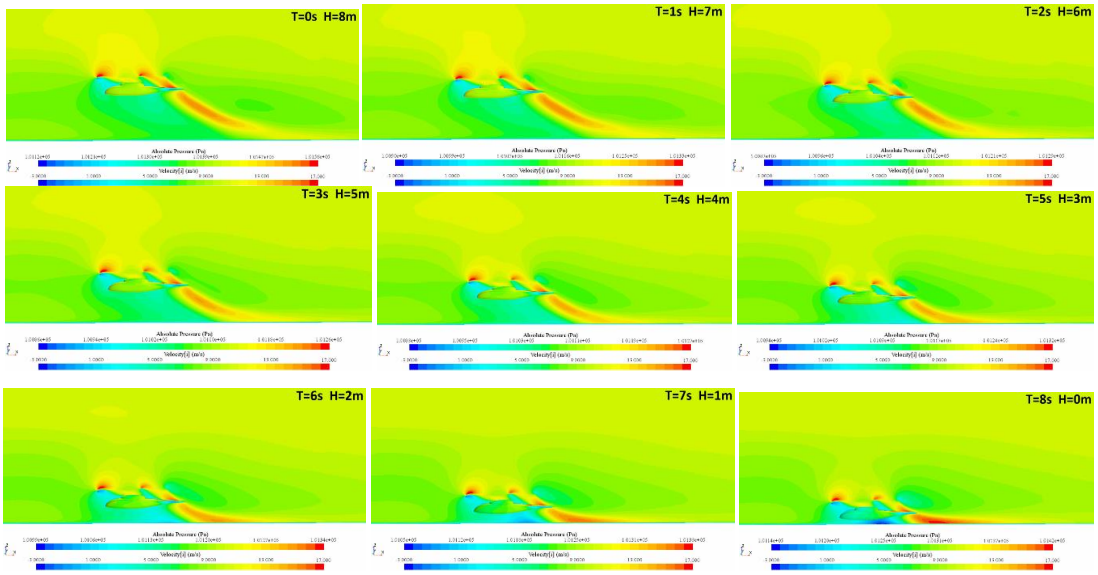

Figure 53-Velocity component V_x distribution during landing

Source: Author

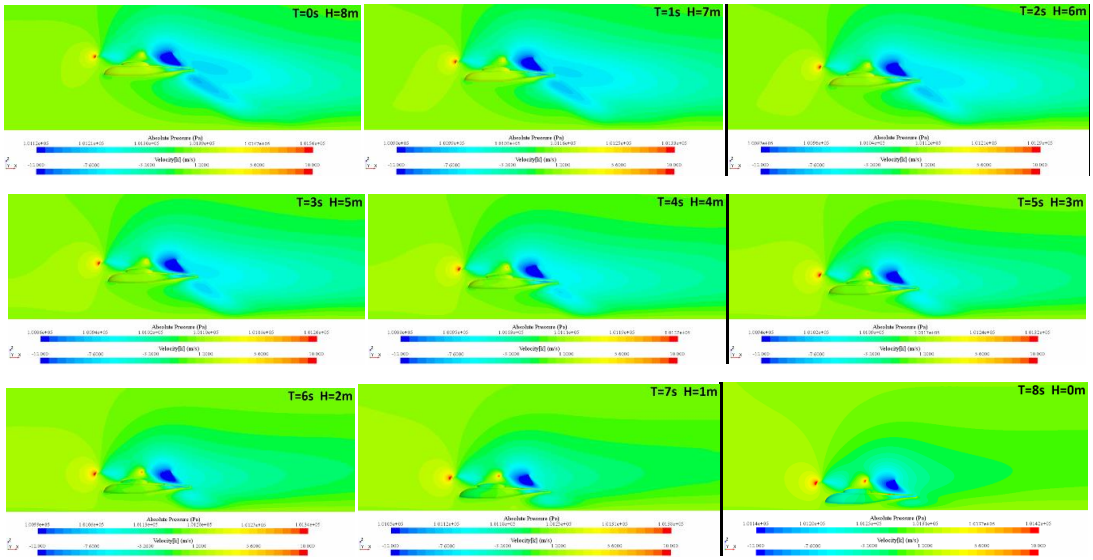

Figure 54-Velocity component V_z distribution during landing

Source: Author

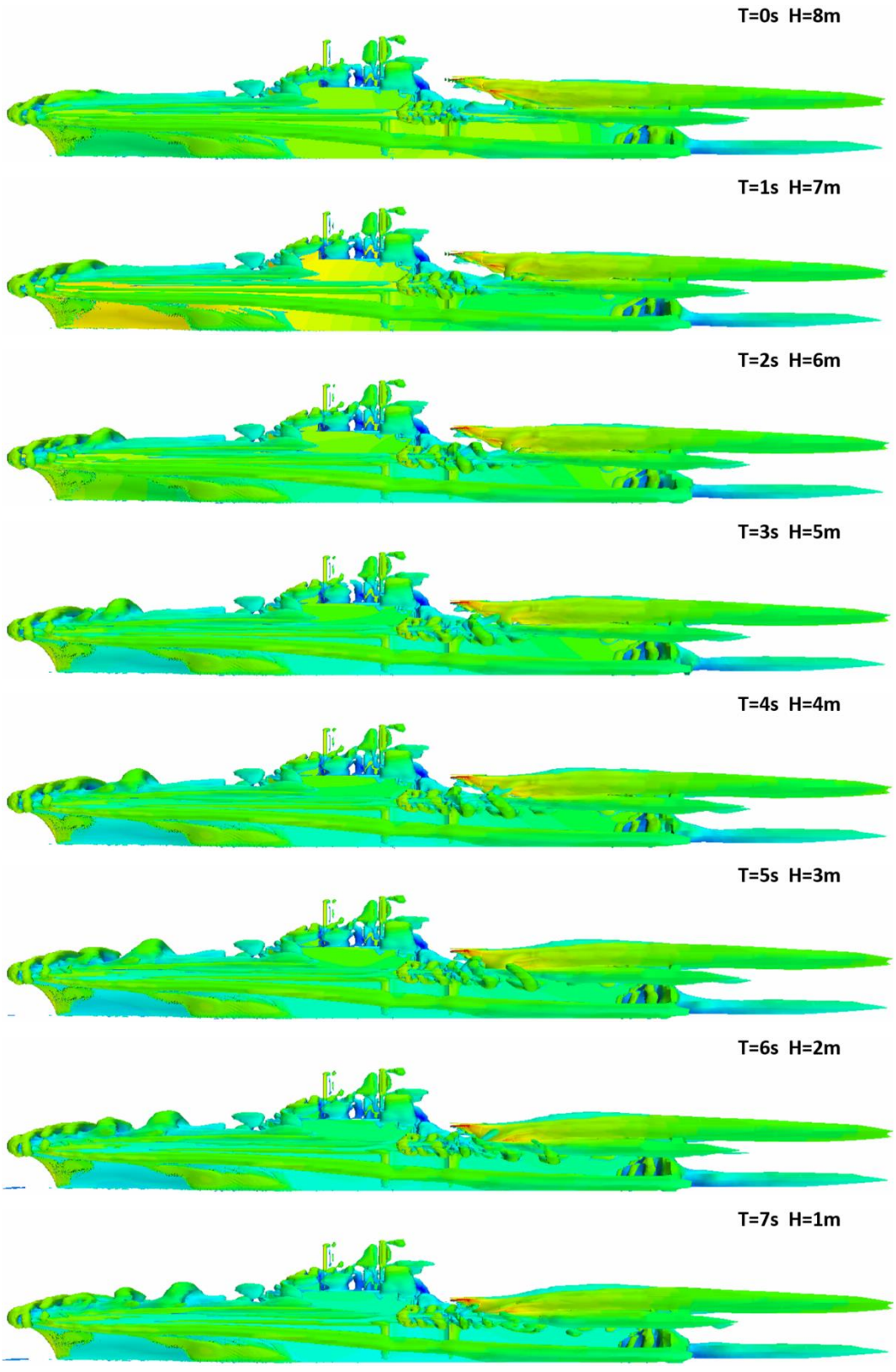
T=0s H=8m
T=1s H=7m
T=2s H=6m
T=3s H=5m
T=4s H=4m
T=5s H=3m
T=6s H=2m
T=7s H=1m

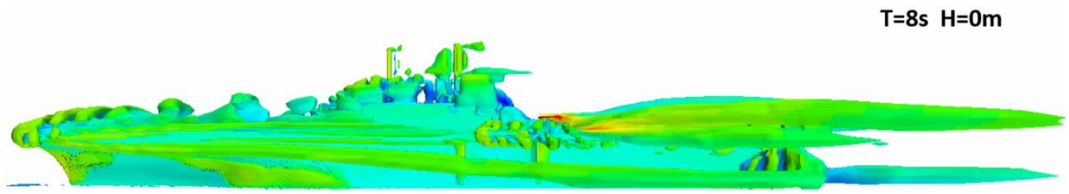

Figure 55-Vortex iso-surface during landing (Q=0.02)

Source: Author

In Figure 53 and 57, the fuselage surface is colored by pressure, no fixed limit. In Figure 55, the iso-surface of vortex extracted by Q is colored by speed, the surface of ship and fuselage is colored by pressure, no fixed limit too. During the landing process, through Figure 53 and Figure 54, the local speed distribution clearly changes. Through Figure 55, the variation of the vortex iso-surface and the time-varying periodic vortex shedding phenomenon can be obtained.

The above results show that the overlapping-virtual disk model successfully captured the dynamic changes of the coupling airflow during the landing.

4.4.5 Helicopter Aerodynamics during landing

Through the coupling simulation, the aerodynamic value of each partcan be obtained. For the convenience of calculation, the helicopter fuselage and tail rotor has been simplified, so the monitored components only include the rotor and fuselage.

There are totally 9 monitoring quantities, including: pulling force of rotor (virtual disk), lateral force, backward force, reactive torque, pitching moment, roll moment, lift force of helicopter, resistance force and lateral force (see 5.1.3 for the different components' aerodynamic force composition). The variation of each monitoring value changing with height is shown in Figure 56, where h is the distance from the bottom of the fuselage to the deck.

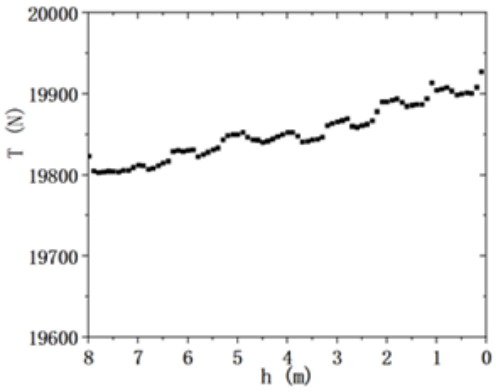

(a) Pulling force of rotor

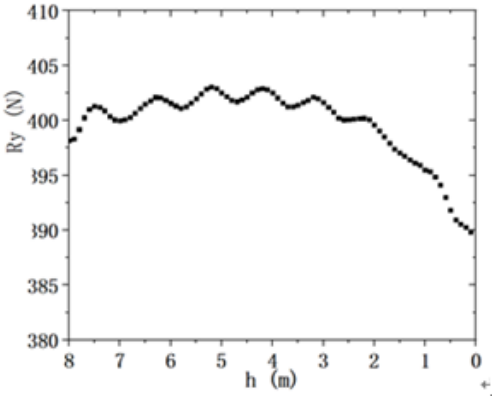

(b) Rotor lateral force

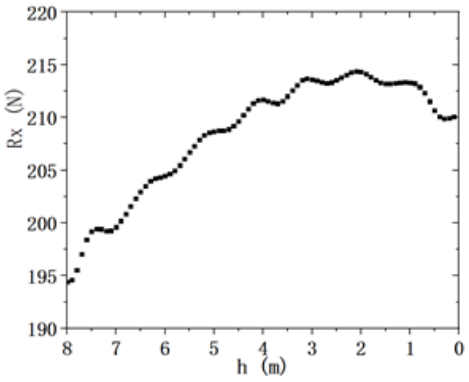

(c) Rotor backward force

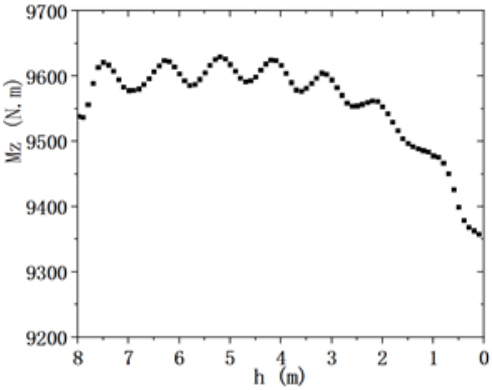

(d) Rotor reactive torque

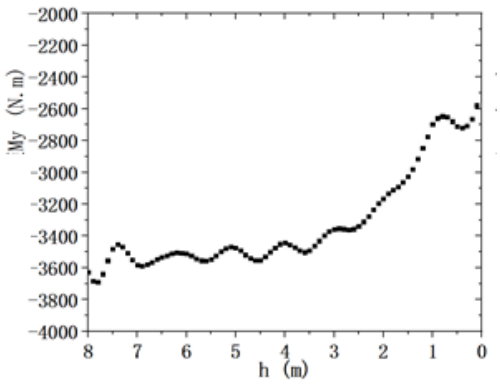

(e) Rotor pitching moment

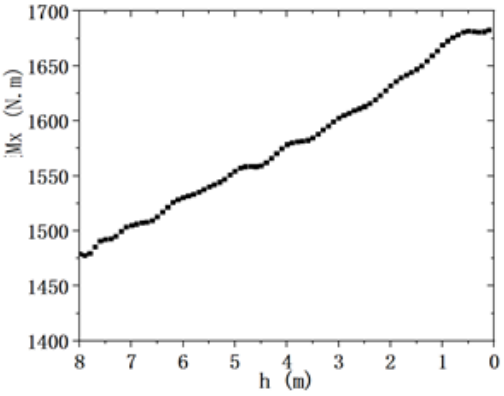

(f) Rotor roll moment

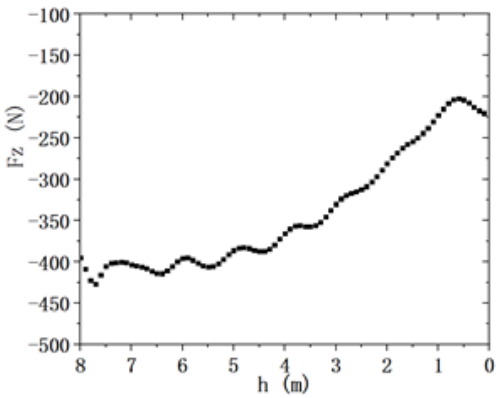

(g) Lift force of helicopter

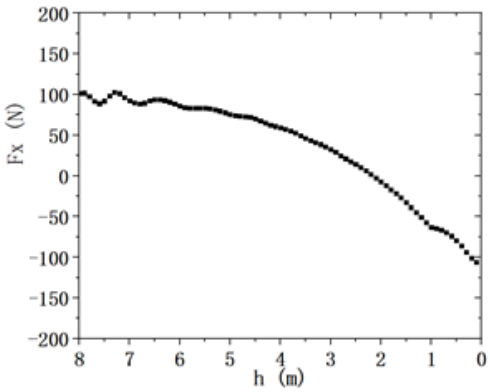

(h) Resistance force

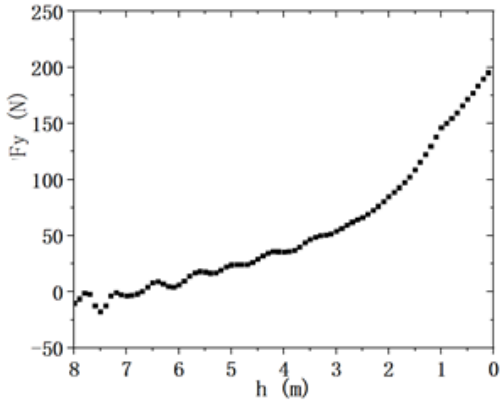

(i) Lateral force of fuselage

Figure 56-Variations of aerodynamic components of fuselage and rotor during landing

Source: Author

In Figure 56(a), rotor lift force generally increases with decreasing of height. This may be related to the "shipboard effect" of ship borne helicopters. Sun Wensheng et al. (2006) points out that when the helicopter flies above the deck, the downwash flow from the rotor strikes the deck, will produce "shipboard effect" similar to the helicopter ground effect. Under the "shipboard effect", the total distance required to produce the same pulling force decreases because the induced velocity decreasing. The lower the hovering height, the stronger the "shipboard effect", the smaller the total distance required to produce the same pulling force. Therefore, if the total rotor

distance is fixed, the closer to the deck, the greater the rotor pulling force will be. Therefore, despite the lack of comparison of different components aerodynamic tests, the research results in Sun Wensheng's paper confirm the rationality of this paper's results to some extent.

In general, the aerodynamic forces and moments of the rotor and fuselage obviously change during landing. This shows that in order to maintain the stability and balance of the helicopter, the pilot needs to constantly adjust the control and attitude angle. Once they exceed the adjustable range, the helicopter may lose control and cause danger.

All of above show that the aerodynamic components changing during landing can be obtained by the overlapping-virtual disk grid.

4.5 Summary

Based on the verification of the interference model, this chapter finishes the numerical simulation of ship-helicopter coupling airflow under 10m/s front inflow, and landing vertically on point E, at a constant speed of 1m/s from 8 meters above the deck. The main conclusions are as follows:

(1) Among the three motion simulation grid schemes, the overlapping-virtual disk grid can reduce the calculation time by 10-20 times compared with the other two, which is more of engineering practicability.

(2) Through the comparison of the fuselage surface pressure data of Robin wing body interference test, the accuracy of using virtual disk model to simulate the helicopter rotor is verified.

(3) Before and after the coupling, the streamline distribution, velocity distribution and pressure distribution of the landing area on deck are very different. The helicopter rotor will form a local air circulation area above the deck, which will

obviously affect the velocity and vortex distribution of the landing area.

(4) The results of vertical velocity distribution in landing area through coupling are obviously different from those obtained by simple superposition of ships and helicopters, which shows the necessity for coupling.

(5) Through the numerical simulation of ship-helicopter coupling airflow, the velocity distribution and vortex change of the helicopter in the landing process are captured successfully.

(6) Through the numerical simulation in this chapter, the dynamic changes of aerodynamic of helicopter components during landing are calculated, which lays a foundation for the dynamic coupling balance calculation and the comprehensive evaluation of the helicopter airflow scheme.

CONCLUSION

Starting from the limitation of the current research in China, this paper studies the numerical simulation of isolated ships and the ship-helicopter coupling airflow, based on "real-time dynamic" and "ship-helicopter coupling", establishes a comprehensive evaluation scheme on the theoretical operation envelope and the take-off and landing safety.

The main conclusions and achievements are as follows:

(1) In the numerical simulation of isolated ship airflow, for the same wind direction, under 5m / s to 30m / s inflow, the velocity distribution of the flow field in most areas, including the landing point, is independent of Reynolds number; under front inflow, six types of vortices will be generated, the first four types of vortices will significantly affect the airflow near the take-off and landing points; under port inflow, the influence of the wind direction change on the velocity distribution is more obvious than that of the starboard; if under starboard inflow and the wind direction changes continuously, the existence of the ship island will lead to the "discontinuity "of the vertical velocity distribution, and have a great influence on the takeoff and landing nearby.

(2) For the coupling simulation, the overlapped-virtual disk grid can reduce the calculation time by 10-20 times compared with the other two schemes and is of engineering practicability. The coupling results are significantly different from simple superposition, which shows the necessity for coupling. Besides, the flow field information and the real-time change of the helicopter aerodynamic components during landing are successfully captured, which shows that the method is feasible.

(3) Based on the balance calculation method of a conventional helicopter, the aerodynamic force of helicopter component are introduced and modified into the

coupling simulation, thus realizing the "ship-helicopter coupling"; the "real-time dynamic" is realized by the sectional calculation of the take-off and landing path and the curve fitting of final balancing component. Therefore, a dynamic coupling balance calculation method for ship borne helicopter taking off and landing is proposed.

In order to make the conclusions and methods more rigorous and intact, further research on the following aspects can be carried out:

(1) Although the author tries to collect test data to verify the accuracy and feasibility of the calculation method as far as possible, due to the serious lack of relevant test data, there are still obvious defects in the accuracy verification of the calculation method in this paper, especifically reflected in:

For isolated ship simulation, there is no comparison of real scale ship's testing data; for the overlapping-virtual disk method used in coupling, only compared with the experimental data of Robin wing body interference model, which can only verify the accuracy of the virtual disk model, but unable to fully verify the accuracy of the overlapping-virtual disk scheme.

(2) Due to the limitation of computational resources, for the proposed comprehensive evaluation airflow scheme, this paper lacks the verification of the intact evaluation process, and no sufficient argument for the feasibility of the evaluation method. For the calculation method of dynamic coupling balance, in particular, the convergence and accuracy of the actual calculation need to be further studied and demonstrated.

(3) In this paper, the 6-DOF swaying and the free surface wave are not considered.

(4) The calculation amount of the comprehensive evaluation scheme proposed in this paper is still quite large. Therefore, how to further improve the efficiency while ensuring the accuracy is still the key problems that need to be solved.

REFERENCE

Alpman, E., Horn, J., & Bridges, D. (2007). *Fully-Coupled Simulations of the Rotorcraft/Ship Dynamic Interface*. Annual Forum Proceedings - AHS International, 2.

Arunajatesan, S., Shipman, J., & Sinha, N. (2004). *Towards Numerical Modeling of Coupled VSTOL-Ship Airwake Flowfields*. Paper presented at the owards Numerical Modeling of Coupled VSTOL-Ship Airwake Flowfields.

Bogstad, M., Ait-Ali, D., Akel, I., Giannias, N., Habashi, W., & Longo, V. (2002). *Computational-Fluid-Dynamics Based Advanced Ship-Airwake Database for Helicopter Flight Simulators*. Journal of Aircraft - J AIRCRAFT, 39, 830-838. doi:10.2514/2.3003

Camelli, F., Sandberg, W., & Ramamurti, R. (2004). *VLES study of ship stack gas dynamics*. doi:10.2514/6.2004-72

Forrest, J., & Owen, I. (2010). *An investigation of ship airwakes using Detached-Eddy Simulation*. Computers & Fluids, 39, 656-673. doi:10.1016/j.compfluid.2009.11.002

Gao, Y. Liu, C.M. & He, Z. *Research on CVN deck vortices structure characteristics caused by wind direction changes*. ACTA Aerodynamica Sinica.31(3), 310-315.

He, S.H., & Liu, D.Y. (2015). *Numerical simulation on unsteady ship airwake*. Journal of Dalian Maritime University. 41(03):67-72+86. doi: 10.16411/j.cnki.issn1006-7736.2015.03.012

Hou, Y.H., Huang, S., Hu, Y.L.& Wang, W.Q. (2012). *Evaluation of Warship Based on Relative Entropy Method*. Journal of Shanghai Jiaotong University, (08):1218-1229. DOI：10.16183/j.cnki.jsjtu.2012.08.008

Johnson, W., Yamauchi, G., Derby, M., & Wadcock, A. (2002). *Wind Tunnel Measurements and Calculations of Aerodynamic Interactions Between Tiltrotor Aircraft*. doi:10.2514/6.2003-47

Lee, Y., & Silva, M. (2010). *CFD-Modeling of Rotor Flowfield Aboard Ship*. Paper presented at the 48th AIAA Aerospace Sciences Meeting Including the New Horizons Forum and Aerospace Exposition.

Lee, R., & Zan, S. (2010). *Wind Tunnel Testing of Unsteady Loads on a Helicopter Fuselage in a Ship Wake.*

Li, P. & Huang, S. (2005). *Analysis and management of risking developing warship equipment.* Journal of Harbin Engineering University. 26(02):147-151.

Liao, Q.M., Huang, S. Wang, Y. &Li, X. (2015). *Human Performance in Vessel Passages Based on Improved TOPSIS Method*. Journal of Southwest Jiaotong University. (03):536-542.

Liu, C.M. (2014). *Numerical Simulation of turbulent wind field around large-scale marine structures.* [Unpublished master's thesis]. Harbin Engineering University.

Liu, C. Y., Ma, Y. Y., Xu, J.& Huang, X.Q. (2009). *Study on quantization evaluation methods for overall efficiency of ship.* Ship Science and Technology. 31(3):51-55.

Lu, C. Jiang, Z.F., & Wang, T. (2009). *A comparison of ships' airwakes with different flight decks.* Ship Science and Technology. 31(7), 29-31. doi:10.3404/j.issn.1672-7649.2009.07.004

Lv, J.W., Qi, H.& Shi, W.J. (2005). *Integrated Evaluation of Warship Design Alternatives Based on Rough Set Theory.* MATHEMATICS IN PRACTICE AND THEORY. 35(11):127-131. DOI: 10.3969/j.issn.1000-0984.2005.11.022

Lv, J.W., Wang, X.L.& Zeng, H.J. (2006). *Research on the Assessment Methodology for Design Alternatives of Navy Vessels*. CHINESE JOURNAL OF SHIP RESEARCH. 11(1):21-24. DOI: 10.3969/j.issn.1673-3185.2006.01.007

Polsky, S. (2003). *CFD Prediction of Airwake Flowfields for Ships Experiencing Beam Winds.* Paper presented at the 21st AIAA Applied Aerodynamics Conference.

Polsky, S., & Bruner, C. (2000). *Time Accurate CFD Analysis of Ship Air Wake with Coupled V-22 Flow.*

Rajagopalan, R., Schaller, D., Wadcock, A., Yamauchi, G., Heineck, J., & Silva, M. (2005). *Experimental and Computational Simulation of a Model Ship in a Wind Tunnel.* Paper presented at the 43rd AIAA Aerospace Sciences Meeting and Exhibit.

Rajmohan, N., Zhao, J., He, C., Kim, J., Sankar, L., & Prasad, J. (2012). *An Efficient POD based Technique to Model Rotor/Ship Airwake Interaction.* Paper presented at the American Helicopter Society 68th Annual Forum.

Silva, M., Yamauchi, G., Wadcock, A., & Long, K. (2020). *Wind Tunnel Investigation of the Aerodynamic Interactions Between Helicopters and Tiltrotors in a Shipboard Environment.*

Su, D.C.,Shi, Y.J., Xu, G.H.& Zong, K. (2017). *Numerical simulatin of coupled flow field of helicopter/ship*. Acta Aeronautica ET Astronautica Sinica. 38(07):80-91. DOI: 10.7527 /S1000-6893.2017.120853

Sun, P., Di, X., Zhao, J.& Zhong, K.J. (2015). *Influence of wind directions on the flow field structures of helicopter rotor and deck*. Journal of Aerospace Power. 30(08):1802-1810. DOI: 10.13224/j.cnki.jasp.2015.08.002

Sun, W.S., Bi. Y.H.& Bai, C.H. (2006). *Research on Shipboard Effect of Naval Helicopter.* AERONAUTICAL COMPUTING TECHNIQUE. (02):9-12. DOI: 10.3969/j.issn.1671-654 X.2006.02.003

Sun, X.Y. (2007). *Reaserch on the calculation domain setting of flow around bluff body*. Wind Engineering Committee of bridge and structural engineering branch of China Civil Engineering Society. 6.

Syms, G. (2004). *Numerical Simulation of Frigate Airwakes*. International Journal of Computational Fluid Dynamics, 18. 199-207. doi:10.1080/10618560310001634159

Tai, T., & Carico, D. (1995). *Simulation of DD-963 Ship Airwake by Navier-Stokes Method.* Journal of Aircraft - J AIRCRAFT, 32, 1399-1401. doi:10.2514/3.46892

Tattersall, P., Albone, C., Soliman, M., & Allen, C. (1988). *Prediction of Ship Air Wakes over Flight Decks using CFD.*

Wadcock, A., Yamauchi, G., Heineck, J., Silva, M., & Long, K. (2004). *PIV Measurements of the Wake of a Tandem-Rotor Helicopter in Proximity to a Ship*. 24.

Wakefield, N. H., Newman, S. J., & Wilson, P. (2002). *Helicopter flight around a ship's superstructure*. Proceedings of The Institution of Mechanical Engineers Part G-journal of Aerospace Engineering - PROC INST MECH ENG G-J A E, 216, 13-28. doi:10.1243/0954410021533391

Xiong, Y.F.,Cai, Z.X.& Chen, Z.L. (2007). *Optimal Choice of Ship Forms Based on the Grey Multi-hierarchical Appraise Model*. JOURNAL OF WUHAN UNIVERSITY OF TECHNOLOGY. 31(2):337-340. DOI: 10.3963/j.issn.2095-3844.2007.02.041

Yamauchi, G., Wadcock, A., & Derby, M. (2003). *Measured Aerodynamic Interaction of Two Tiltrotors.*

Zan, S. (2002). *Experimental Determination of Rotor Thrust in a Ship Airwake*. Journal of the American Helicopter Society, 47. doi:10.4050/JAHS.47.100

Zan, S. (2003). *Technical Comment on "Computational-Fluid-Dynamics Based Advanced Ship-Airwake Database for Helicopter Flight Simulation"*. Journal of Aircraft - J AIRCRAFT, 40, 1007-1007. doi:10.2514/2.6890

Zhang, X. Y., Chang, X., Li, X.& Yang, F.Q. (2016). *Evaluation method of airflow field plan in warship based on improved ELECTRE method.* Journal of Beijing University of Aeronautics and Astronautics. 42(11):2507-2515. DOI: 10.13700/j.bh.1001-5965.2015.0703

Zhao, Y.Z. (2012). *Numerical Simulation of Steady and Unsteady Air Flow Field around Large Ship.* [Unpublished master's thesis]. Harbin Institute of Technology.